Counterflow heat exchanger design for the E-ELT METIS instrument cooler

Master Thesis Applied Physics

by E. Dollekamp

Energy, Materials and Systems group
University of Twente
Enschede, The Netherlands
February 26, 2014

Committee:
Prof. dr. ir. H.J.M. ter Brake
Prof. dr. R.M. van der Meer
Dr. ir. S. Vanapalli
Ing. H.J. Holland

UNIVERSITY OF TWENTE.

Abstract

This master thesis discusses the design of the final stage of the METIS detector instrument cooler for the European Extremely Large Telescope. The final stage is the lowest temperature part of the helium stage of the cooler. The final stage exists out of a counterflow heat exchanger, a Joule-Thomson throttle and a final stage heat exchanger. This final stage is the most critical part of the cooler. The counterflow heat exchanger needs to have an effectiveness of 99.8% and the final stage heat exchanger must deliver a cooling power of 0.4 W at 8 K. Different types of counterflow heat exchangers are analyzed. Modeling indicates that long lengths of counterflow heat exchangers are required. A tube-in-tube counterflow heat exchanger needs a length of 17.16 m and a coiled finned tube counterflow heat exchanger needs a length of 9.85 m. The final stage heat exchanger can be relatively short with a length of 1 m and the Joule-Thomson throttle needs to be a small restriction in the μm range. The final stage experimental setup has been designed but due to the limited time span of the research the setup has not yet been manufactured. Instead a setup has been manufactured to measure the effectiveness of a counterflow heat exchanger. The effectiveness of a 3.02 m long tube-in-tube counterflow heat exchanger has been determined. At a mass flow of 99.62 mg/s the effectiveness resulted in 93.05±1.10%. This agrees with the modeled effectiveness of 93.10%. At lower mass flow the effectiveness increases but also the error in the measurement due an observed radiation heat inleak. A longer tube-in-tube CFHX and other type of counterflow heat exchangers still need to be manufactured and tested in an effectiveness characterization setup with lower radiation heat inleak.

Acknowledgments

Off course this master thesis would not be possible without the help and effort of several people. Starting off with supervisor Y. Wu, who was always very helpful when I had questions. I would also like to thank head supervisor H.J.M. ter Brake for guidance and sharing insight in physical aspects relating the final stage. Then I also want to thank C.H. Vermeer and H.J. Holland for helping me out in the lab and giving me insight in the practical aspects relating the final stage. Finally I want to thank the committee members and all the other colleagues of the Energy, Materials and Systems research group which were all really friendly and helpful throughout the project. I had a great time in the group.

Contents

Chapter 1

Introduction

In 2022 the European Southern Observatory (ESO), a 15-nation intergovernmental research organization for astronomy, is planning to complete the European Extremely Large Telescope (E-ELT) [1]. This ground-based telescope will be built on a mountain top in Cerro Armazones, Chile. With a 39.3 m diameter primary mirror it will be the largest telescope in the world, see figure 1.1. It is providing images 16 times sharper than those from the Hubble Space Telescope. The E-ELT covers the optical/near-infrared range and its purpose is to get detailed information about exoplanets, first stars, galaxies, dark matter and dark energy. Two platforms with the size of tennis courts are available for analyzing instruments [2]. One of these platforms is depicted in figure 1.2. The incoming light of the telescope is analyzed by a total of eight instruments. One of these eight instruments is the Mid-infrared E-ELT Imager and Spectrograph (METIS). METIS will open up a huge discovery space at mid-infrared wavelengths, a region that is thus far relatively unexplored. Science drivers for METIS are for example the physical and chemical properties of exoplanets and the growth of supermassive black holes [3]. The METIS instrument is also depicted in figure 1.2. It will be placed inside a sphere which is surrounded by liquid nitrogen. This liquid nitrogen will be pumped down to a temperature of 70 K.

The METIS instrument needs to be cooled down to cryogenic temperatures. At these low temperatures the detector performs better since the instrument will encounter less noise signals. To further reduce the noise it is also important that the instrument operates vibration free. Mechanical coolers like pulse-tube- and Gifford-McMahon (GM) coolers cause a lot of vibrations. An alternative for these vibrating mechanical coolers are sorption-based coolers. Sorption-based coolers offer vibration-free, long-life operation with minimum maintenance and no-op periods [6]. The University of Twente has over 10 years experience in developing sorption-based cooling techniques. The sorption coolers were mainly developed for detectors of space missions, which require low cooling powers in the order of a few milliwatts. The detectors of the METIS instrument require much higher cooling powers in the order of 0.4 - 1.4 W. A baseline E-ELT METIS sorption cooler has been designed and is depicted in figure 1.3. The baseline design has four temperature levels: a N-band detector at 8 K, optics at 25 K, a L/M-band detector at 40 K and optics at 70 K. The detectors analyze specific wavelengths in the infrared. These specific wavelengths are called ”bands”. The bands covered are the L (3.0 - 4.0 μm), M (4.6 - 5.0 μm) and N (7.5 - 14.5 μm) band. To establish these temperature levels three cascaded Joule-Thomson coolers are used. A helium-operated cooler is used to obtain the 8 K level. At this temperature it has to

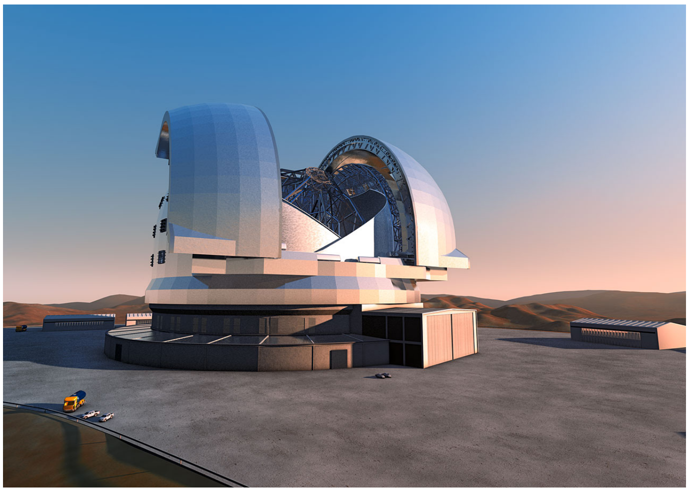

Figure 1.1: An artist's impression of the E-ELT [4].

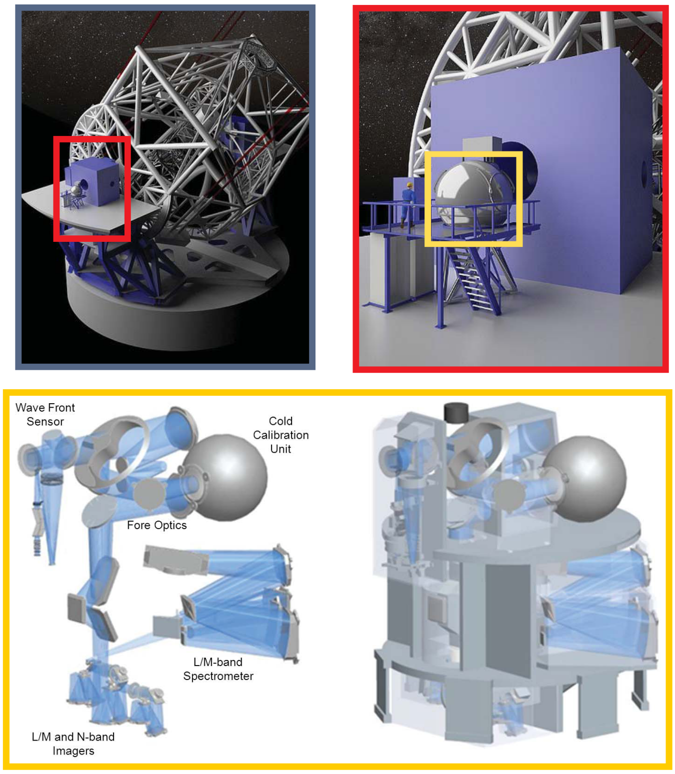

Figure 1.2: A schematic of the platform and the METIS instrument [5].

Table 1.1: Values helium stage baseline optimization METIS cooler [7, 8].

Variable	Symbol	Value
Mass flow rate	$\dot{m}$	100.03 mg/s
Pressure of the high-pressure channel	p_H	14.32 bar
Pressure of the low-pressure channel	p_L	7.46 bar
Cooling power	P_{cool}	0.4 W
Cooling temperature	$T_{Final\,Stage\,HX}$	8 K
Temperature stability	–	< 10 mK

deliver a cooling power of 0.4 W to the N-band detector and the temperature stability needs to be < 10 mK [7]. The 15 K and 25 K stages are provided by a hydrogen-based cooler and the 40 K stage is realized by a neon-based cooler. The 70 K is obtained by a pumped-liquid nitrogen line. In figure 1.3 these three cascaded cooling chains are depicted.

A sorption cooler operates in a thermodynamic cycle. A temperature-specific entropy (T-s) diagram of an ideal helium final stage cycle is shown in figure 1.4. In a sorption cooler gas is adsorbed by carbon pills in a sorption cell. This is done at low temperature and pressure. When heating up the cell, the gas will desorb at high temperature and pressure. This warm high-pressure gas will cool down in a counterflow heat exchanger (CFHX), see the red line in figure 1.4. The gas will cool down very close to 8 K since the CFHX is 99.8% effective. The cooled down high-pressure gas will adiabatically expand through a Joule-Thomson (JT) throttle, this happens at the green line in figure 1.4. It can be seen in the diagram that this is an isenthalpic process. After the expansion the gas has lowered in temperature and pressure. The gas can now absorb heat from the detector in the final stage heat exchanger, this is the blue line in figure 1.4. After absorbing heat from the detector the gas flows back through the CHFX, cooling the incoming warm high-pressure gas. This can be seen by the purple line in figure 1.4. After flowing through the CFHX, the gas is adsorbed again by the sorption cell and the cycle can start all over.

The final stage is the bottom part of the helium cooler. In figure 1.3 the final stage is circled in red. The final stage consists of a CFHX, a JT-throttle and a final stage heat exchanger (HX). Pre-cooled high-pressure helium gas of 15 K enters the final stage. In the CFHX the helium is cooled down to 8 K. Adiabatic expansion through the JT-throttle further cools down the gas to 7.48 K. In the final stage HX the helium gas absorbs 0.4 W of heat from the detector and heats up again to 8 K. The low-pressure gas then flows back through the CFHX where it cools the incoming high-pressure gas. The specifications of the cooler are listed in table 1.1.

Sensitivity analysis of Y. Wu indicates that the CFHX of the final stage is the most critical part of the METIS cooler. This analysis investigates how the effectiveness of a specific CFHX influences the total heating input power of the cooler. In the analysis of a specific CFHX all the other CFHXs in the system are assumed to operate ideal. The sensitivity analysis for the CFHX in the final stage is given in figure 1.5. In this figure the sensitivity is the slope of the fitted line. The more the 'Total heating input power' rises when there is a change in effectiveness the higher its sensitivity. A sensitivity analysis is done on all CFHXs in the cooler. The sensitivity of the other CFHXs normalized to the sensitivity of the final stage CFHX are given in table 1.2. From this table it can be concluded that the CFHX in the final stage is the most critical CFHX.

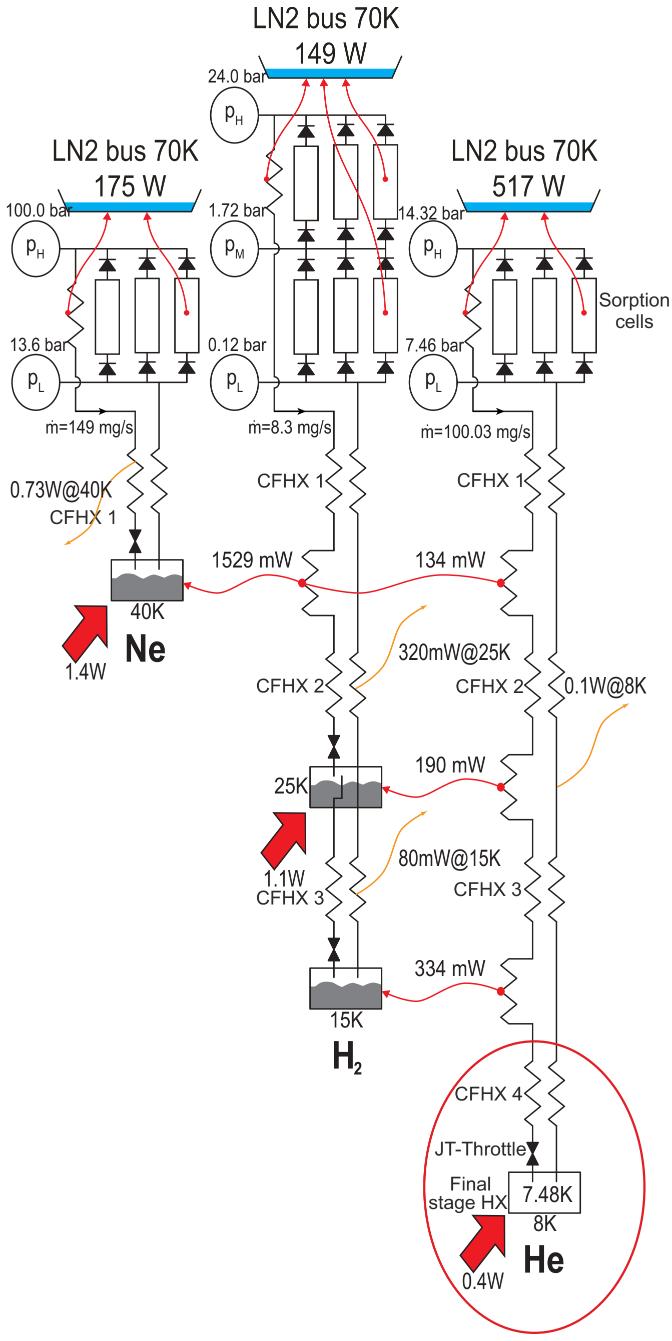

Figure 1.3: Baseline E-ELT METIS sorption cooler chain scheme [6].

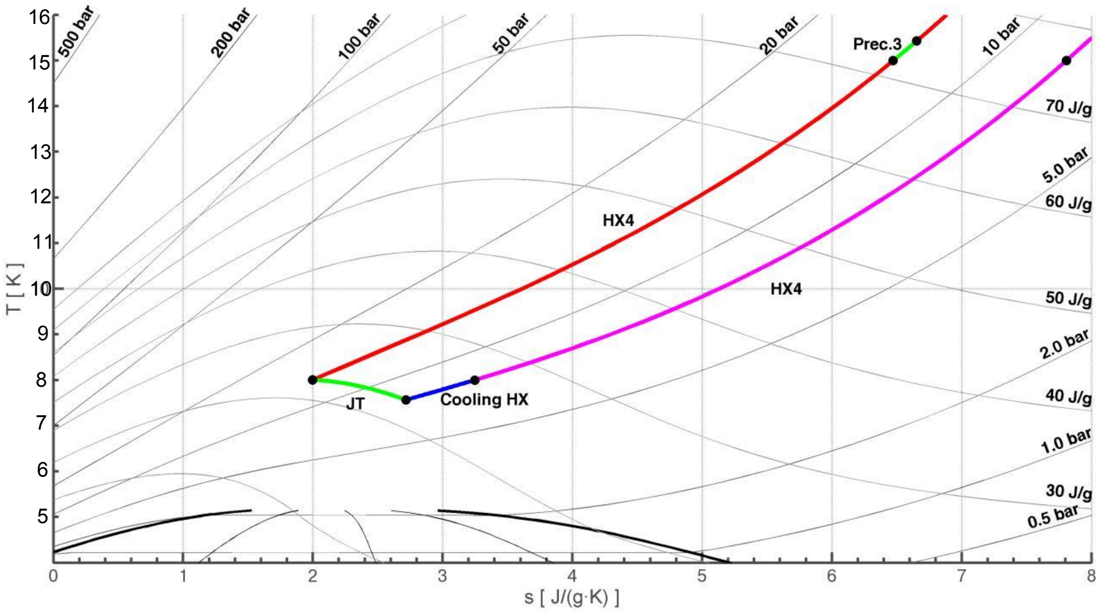

Figure 1.4: T-s diagram of the final stage [6].

Hydrogen stage CFHX 2 and helium stage CFHX 2 are not listed in the table since a small change in effectiveness in these CFHXs does not change the input power. This is due to the cooling capacity margin of the 25 K stage of the hydrogen cooling chain [8]. The ideal input power when all CFHXs are 100% effective is 713.67 W [8]. The acceptable minimum effectiveness of the CFHX is evaluated for a 1.5% increase of input power. The final stage CFHX in this case needs to have an effectiveness higher than 99.8% to fulfill this requirement. Due to this high requirement, the master thesis is devoted to the design of the final stage. The thesis starts with a theory section in which parasitic heat losses, the principles of a CFHX, the JT-throttle and the final stage HX are described. The thesis then continues with a chapter wherein models of different kinds of CFHXs are explained. After this an analysis of the final stage characterization setup has been performed. The thesis then continues with explaining the CFHX effectiveness measurement setup. After this chapter the results of the different analyses are shown. The thesis ends with a discussion and conclusion.

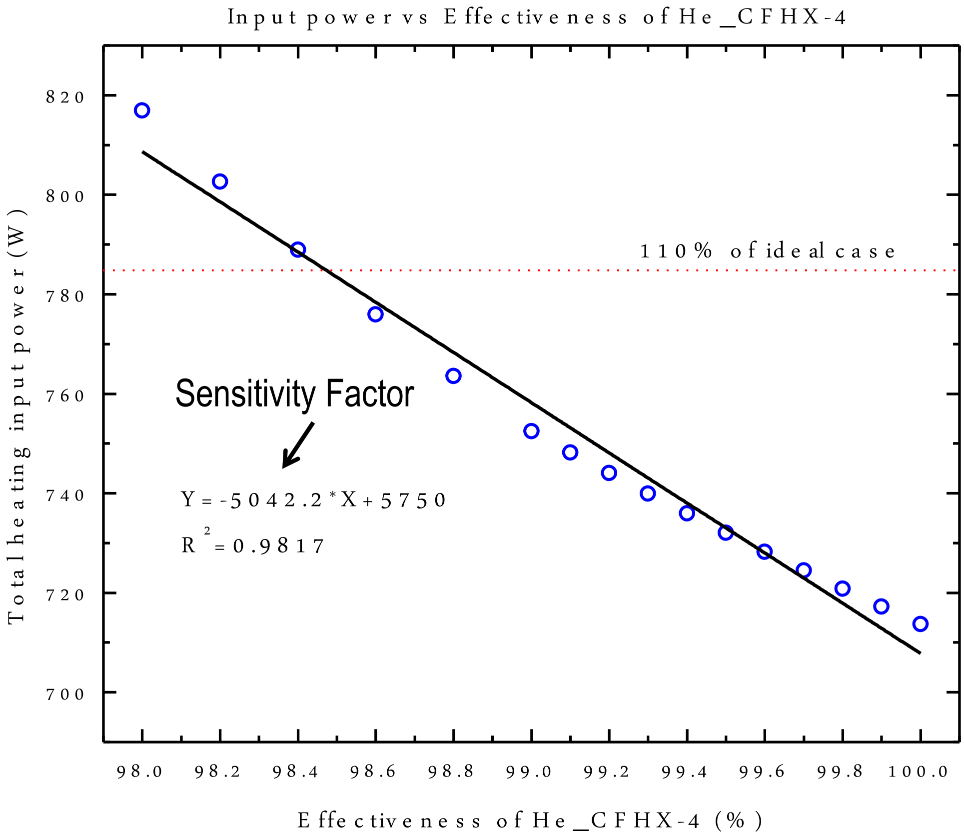

Figure 1.5: Sensitivity analysis of the CFHX in the final stage [8].

Table 1.2: Sensitivity analysis results [8].

CFHX	Influence of CFHX effectiveness on required input power relative to the effectiveness of CFHX 4
Neon stage CFHX	0.049
Hydrogen stage CFHX 1	0.026
Hydrogen stage CFHX 3	0.084
Helium stage CFHX 1	0.154
Helium stage CFHX 3	0.659
Helium stage CFHX 4	1.000

Chapter 2

Theory

In this chapter the theory behind the different parts of the final stage is treated. The chapter starts with introducing some general concepts encountered when dealing with cryogenics. The chapter then continues with the principles of a CFHX, JT-throttle and the final stage HX.

2.1 Parasitic heat losses

When dealing with cryogenic systems it is important to take into account parasitic heat losses. Parasitic heat losses have a negative effect on the performance of a cooler. Therefore the parasitics need to be minimized. Different types of parasitic heat losses and how they can be reduced are described in this section.

2.1.1 Conduction

Thermal conduction is the heat transfer through a material without any motion of the material as a whole. The conduction is given by:

$$\dot{Q}_{con} = \frac{A}{L} \int \lambda(T) dT. \tag{2.1}$$

In this equation A is the cross-sectional area, L is the length and λ is the thermal conductivity of the material, which is dependent on the temperature of the material. From equation (2.1) it follows that a small A, a small λ, a small temperature difference and a large L reduce the conduction through a material. The thermal conductivity is linearly proportional to the electrical conductivity. This relation is given by the Wiedemann-Franz law:

$$\frac{\lambda}{\sigma} = LT, \tag{2.2}$$

where σ is the electrical conductivity of the material and L is the Lorenz number which has a value of $2.44 \cdot 10^{-8}$ WΩK^{-2}. A good electrical conductivity results into a good thermal conductivity. Sensor wiring in cryogenic systems is often done with manganin wire. This is a thin wire with an acceptable thermal conductivity (2 W$\cdot$m$^{-2}\cdot$K^{-4} @10 K [9]) and an acceptable electrical conductivity. Wires are also often thermally anchored to pre-cooling stages of the cooler. This lowers the temperature difference in the wire.

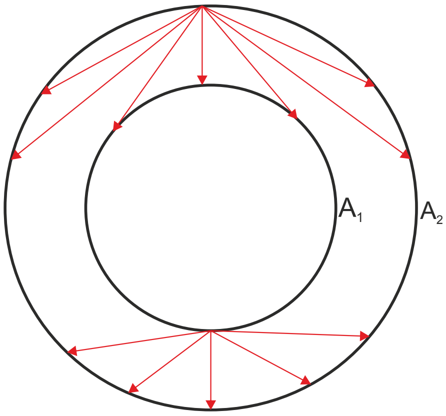

Figure 2.1: Explanation of the view factor.

2.1.2 Radiation

Radiation is the heat inleak caused by electromagnetic radiation. All surfaces radiate heat. The higher the temperature of the surface the higher its radiation. Radiation does not need a medium to propagate and thus can even propagate through vacuum. The amount of radiation between two surfaces (1 and 2) is given by equation (2.3) [10].

$$\dot{Q}_{rad_{2\to1}} = \frac{\sigma(T_2^4 - T_1^4)}{\frac{1-\varepsilon_1}{\varepsilon_1 A_1} + \frac{1}{A_2 F_{21}} + \frac{1-\varepsilon_2}{\varepsilon_2 A_2}} \tag{2.3}$$

In this equation σ is the Stefan-Boltzmann constant which is 5.67×10^{-8} $\mathrm{Wm^{-2}K}$, ε is the surface emissivity and F_{21} is the view factor. The surface emissivity is the ability to emit energy by radiation. It is the ratio of energy radiated by the surface to energy radiated by a black body at the same temperature. The view factor F_{21} is the proportion of radiation leaving surface 2 to that arriving at surface 1. The view factor holds the following reciprocity relationship: $A_1F_{12} = A_2F_{21}$. In figure 2.1 this view factor is explained in case of an enclosed surface. All radiation leaving surface A_1 falls on surface A_2, so the $F_{12} = 1$. This is not the case when the radiation leaves surface A_2. Here some part of the radiation is falling on A_1 and some radiation is falling back again on A_2. For obtaining the view factor F_{21}, the reciprocity relationship can be used. This results in $F_{21} = \frac{A_1}{A_2}$. Inserting this expression into equation 2.3 results in:

$$\dot{Q}_{rad_{2\to1}} = \frac{\sigma\left(T_2^4 - T_1^4\right)}{\frac{1-\varepsilon_1}{\varepsilon_1 A_1} + \frac{1}{A_1} + \frac{1-\varepsilon_2}{\varepsilon_2 A_2}}. \tag{2.4}$$

The amount of radiative heat transfer on a cooler surface A_1 is proportional to the surrounding temperature T_2^4. It is therefore important that a cooler with temperature T_1 and surface A_1 is surrounded by a surface A_2 with a low temperature T_2. This is done with so called 'thermal radiation shields'. These are shields made from low emissivity materials which are also cooled down to cryogenic temperatures. Changing for example the surrounding temperature of a 30 K cooler from 300 K to 70 K, decreases the radiation by a factor of 349.

Table 2.1: Explanation variables of equation (2.5) [11].

Symbol	Variable	Value
N	Layer density	30 layers/cm
N_s	Total numbers of layers	-
ε_{tr}	Room temperature surface emissivity	0.031
C_s	Empirical constant	2.11×10^{-9}
C_r	Empirical constant	5.39×10^{-10}

2.1.3 Multi-Layer Insulation

To lower radiation onto a cryogenic setup, a setup can be wrapped with Multi-layer Insulation (MLI). MLI is composed out of multiple reflective layers with low conductivity spacers in between. The amount of radiation between two surfaces (1 and 2) with MLI in between is given by equation (2.5) [11]:

$$\dot{Q}_{MLI} = A\frac{1}{2}\frac{C_s N^{3.56}}{N_s + 1}\left(T_2^2 - T_1^2\right) + \frac{C_r \varepsilon_{tr}}{N_s}\left(T_2^{4.67} - T_1^{4.67}\right), \tag{2.5}$$

where an explanation of the variables is given in table 2.1.

2.2 Counterflow heat exchangers

In a CFHX two separate gas streams exchange heat. These gas streams are separated by a solid wall. The cold gas stream absorbs heat from the hot gas stream. This process is schematically depicted in figure 2.2. The temperatures used in this figure are explained in table 2.2. The two channels in a CFHX often have a different pressure. The in- and outlets of the high-pressure line (p_{pH}) and low-pressure line (p_{pL}) are also depicted in figure 2.2. The inlet temperatures T_{pH} and T_{pL} indicated by the green dot, can be considered fixed. Due to the heat transfer between the gas streams, a temperature difference can be established between both sides of the CFHX. CFHXs are mostly made from stainless steel since it has a good thermal conductivity (0.8 W·m^{-1}·K^{-1} @10 K and 16 W·m^{-1}·K^{-1} @300 K [9]). This results in a good heat transfer between the hot- and cold channel of a CFHX. This also means that heat transfer along the tube is good, but making the cross sectional area small and the length long reduces the conductive heat transfer in longitudinal direction.

2.2.1 Different types of CFHXs

There are different configurations possible when looking at two gas stream separated by a solid wall which exchange heat with each other. In this subsection two CFHXs are introduced. Namely the tube-in-tube CFHX and the coiled finned tube CFHX.

Tube-in-tube CFHX

A commonly used CFHX in cryogenics is the tube-in-tube CFHX. The tube-in-tube CFHX consist of two concentric tubes, see figure 2.3. The warm high-pressure gas flows inside the inner tube and the cold low-pressure gas flows through the annular gap, the channel between the inner- and outer tube. It is important to note that the

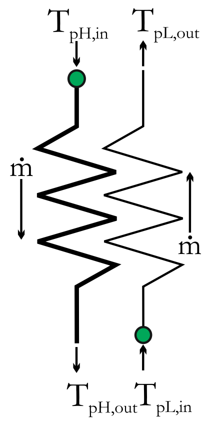

Figure 2.2: Schematic of a CFHX.

two gas streams flow in opposite directions. This flow configuration increases the heat transfer. The tube-in-tube CFHX is often wound to a spiral to make it more compact.

Coiled finned tube CFHX

Another configuration is the coiled finned tube CFHX. The coiled finned tube CFHX is also sometimes referred to as a Giauque-Hampson heat exchanger, named after the inventor of the heat exchanger. In a coiled finned tube CFHX a finned tube is coiled around an inner mandrel, which is then fitted inside an outer tube. The hot high-pressure gas will flow inside the finned tube and the cold low-pressure gas will flow around the finned tube, between the inner mandrel and outer tube. The fins increase the heat transfer area and thus the overall heat transfer. A schematic of the coiled finned tube CFHX is given in figure 2.4. Actually the flow in this kind of heat exchangers is crossflow, but for simplicity it is called a CFHX in this thesis. The coiled finned tube CFHX is often used in high power cryogenic coolers. For example in the Daikin GM-JT Cryocooler from Janis and Sumitomo which can deliver a cooling power of 5 W @4.3 K [13, 14] and the DSN maser cooler from the Jet Propulsion Laboratory which can deliver a cooling power of 1 W @4.5 K [15]. Pictures of both coolers are given in figure 2.5. The advantage over a tube-in-tube CFHX is that the coiled finned tube CFHX can be made more compact.

2.2.2 CFHX effectiveness

The performance of a CFHX can be expressed in terms of effectiveness. The CFHX effectiveness ϵ is defined as the ratio of heat transferred in the actual CFHX to the maximum heat transfer possible that would happen in an ideal CFHX:

$$\epsilon = \frac{\text{actual heat transfer rate}}{\text{maximum heat transfer rate}} = \frac{\dot{Q}}{\dot{Q}_{max}}. \tag{2.6}$$

When a CFHX has an effectiveness of 100%, it is meant that $\epsilon = 1$. In the ideal case

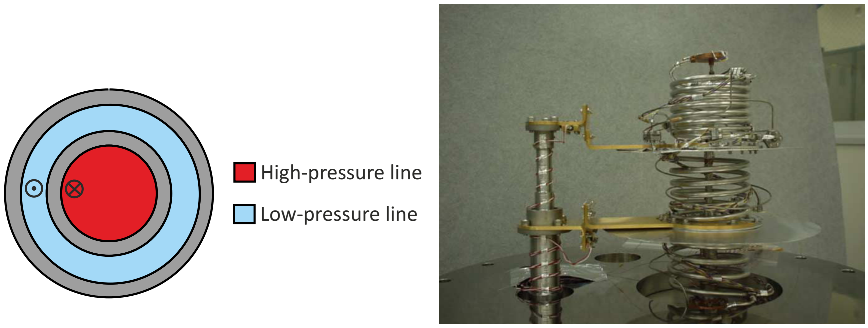

(a) (b)

Figure 2.3: (a): A schematic of a tube-in-tube CFHX, (b): A tube-in-tube CFHX used in a cryogenic setup [12].

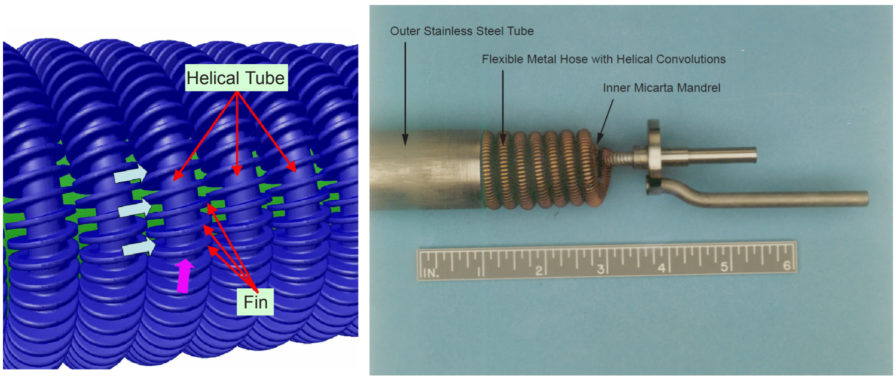

(a) (b)

Figure 2.4: (a): A schematic of a coiled finned tube CFHX [16], (b): A coiled finned tube CFHX [15].

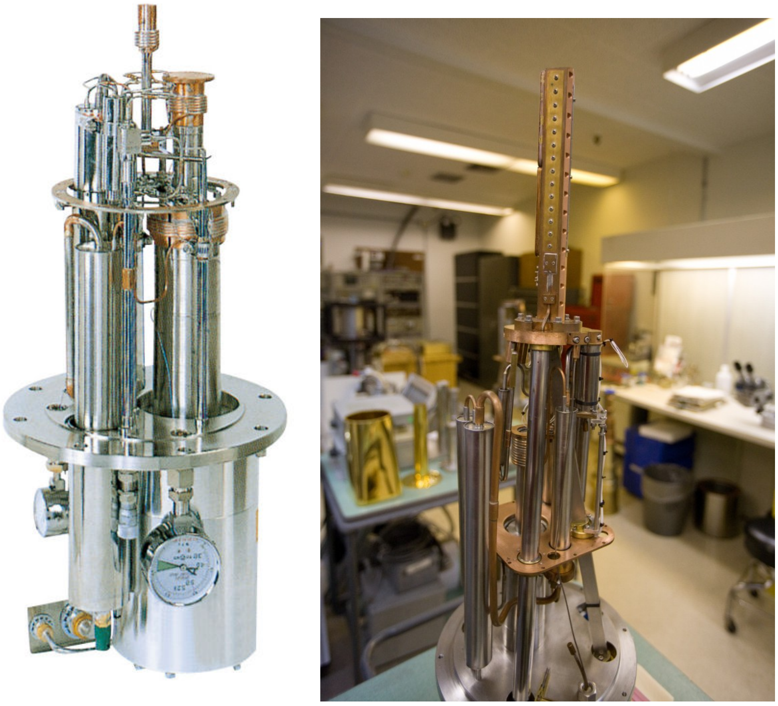

(a) (b)

Figure 2.5: (a): The Daikin GM-JT Cryocooler [13], (b): The GM/JT cooler of the Jet Propulsion Laboratory (JPL) [17].

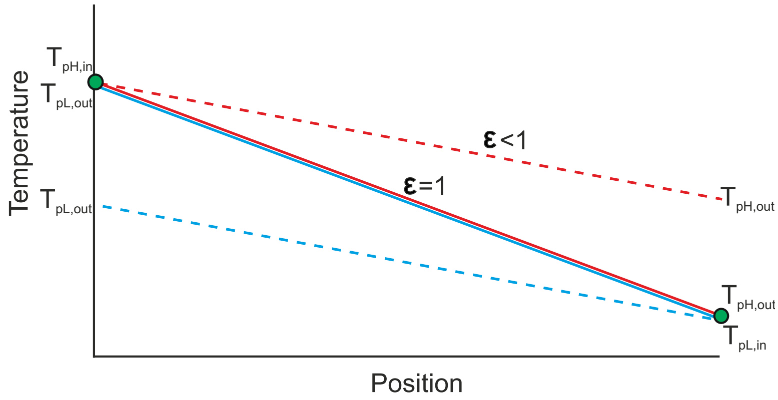

Figure 2.6: Temperature profile at high and low effectiveness.

Table 2.2: Definition of temperatures points.

Variable	Definition
$T_{pH,in}$	Incoming temperature of the high-pressure line
$T_{pH,out}$	Outcoming temperature of the high-pressure line
$T_{pL,in}$	Incoming temperature of the low-pressure line
$T_{pL,out}$	Outcoming temperature of the low-pressure line

of $\epsilon = 1$, all heat from the high-pressure gas stream is transferred to the low-pressure gas stream and $T_{pH,out} = T_{pL,in}$ and $T_{pL,out} = T_{pH,in}$. In a non-ideal CFHX not all heat is transferred from the low- to the high-pressure stream and $\epsilon < 1$, resulting in $T_{pH,out} > T_{pL,in}$ and $T_{pL,out} < T_{pH,in}$. Figure 2.6 shows a temperature profile versus length plot of both an ideal and non-ideal CFHX. Here the red line represents the high-pressure line and the blue line represents the low-pressure line. The green dots represent the same position in the CFHX as the green dots in figure 2.2. In the ideal case (the solid lines) the temperatures of both lines are equal along the length and thus the lines overlap. In the non-ideal case (dashed line) there is less heat transfer and the lines do not overlap but still go parallel. In this plot the specific heat capacities (c_p) of both gas streams are assumed to be equal. When the heat capacities of the two streams are in the ideal case not equal, the line do not go parallel anymore and there will be a temperature difference between $T_{pH,out}$-$T_{pL,in}$ or $T_{pL,out}$-$T_{pH,in}$. This is because the lowest capacity stream limits the total heat transfer. Note that in reality the temperature profile will not be strictly linear but slightly curved due to temperature dependence of the specific heat. The effectiveness can also be expressed in terms of enthalpy flow rate ($\dot{H}$) or specific enthalpy (h):

$$\epsilon = \frac{\dot{Q}}{\dot{Q}_{max}} = \frac{\dot{H}_{T_{pL,out}} - \dot{H}_{T_{pL,in}}}{\dot{H}_{T_{pH,in}} - \dot{H}_{T_{pL,in}}} = \frac{\Delta\dot{H}_{pL}}{\Delta\dot{H}_{max}} = \frac{\dot{m}\left(h_{T_{pL,out}} - h_{T_{pL,in}}\right)}{\dot{m}\left(h_{T_{pH,in}} - h_{T_{pL,in}}\right)} = \frac{h_{T_{pL,out}} - h_{T_{pL,in}}}{h_{T_{pH,in}} - h_{T_{pL,in}}} = \frac{\Delta h_{pL}}{\Delta h_{max}}, \tag{2.7}$$

where $h_{(T,P)}$, which is dependent on temperature and pressure, can be obtained from the computer program REFPROP. The actual enthalpy change in equation (2.7) could as well be expressed as $\Delta\dot{H}_{pH}$ since:

$$\Delta\dot{H}_{pH} = \Delta\dot{H}_{pL}. \tag{2.8}$$

When the c_p's of both gas streams are not equal an adapted version of equation (2.7) needs to be used. This adapted equation is given by equation (2.9). The maximum enthalpy change needs to be evaluated at both pressures and the minimum has to be taken.

$$\epsilon = \frac{\Delta h_{pL}}{min\left[\Delta h_{max(pH)}, \Delta h_{max(pL)}\right]} \tag{2.9}$$

The effectiveness can also be obtained by the following equation:

$$\epsilon = 1 - \frac{\dot{H}_{pH_{out}} - \dot{H}_{pL_{in}}}{\Delta\dot{H}_{max}} = 1 - \frac{\dot{Q}_{cool}}{\Delta\dot{H}_{max}}, \tag{2.10}$$

so by measuring the cooling power $\dot{Q}_{cool}$ to go from $\dot{H}_{pH_{out}}$ to $\dot{H}_{pL_{in}}$ the effectiveness of the CFHX can be obtained.

2.2.3 Influence of radiation onto a CFHX

During measurements which are presented in upcoming chapters radiation heat inleak was observed. When radiation falls onto the low-pressure line of a CFHX, see also figure 2.7, equation (2.8) does not hold anymore. The new energy balance equation becomes:

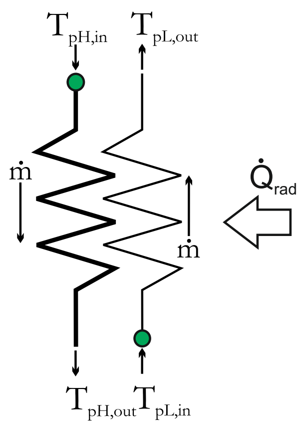

Figure 2.7: Schematic of a CFHX with radiation.

$$\Delta\dot{H}_{pH} + \dot{Q}_{rad} = \Delta\dot{H}_{pL}. \tag{2.11}$$

Here the low-pressure line is warmed up by heat from the high-pressure line and by radiative heat coming from the environment. From equation 2.11 it follows that the low-pressure line has a higher enthalpy change than the high-pressure line. Such a

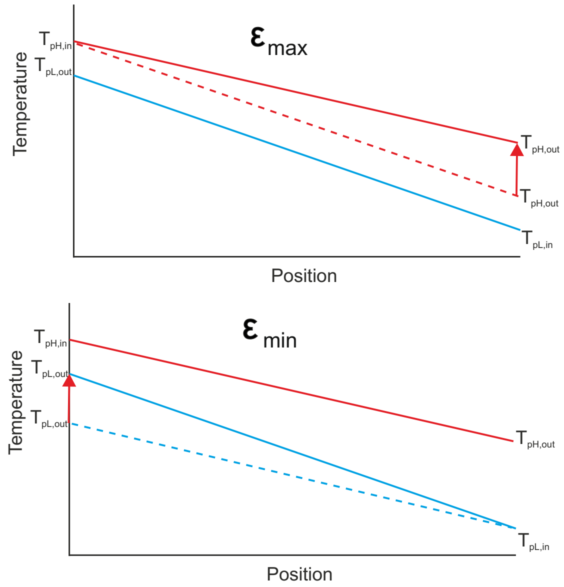

Figure 2.8: Schematic of a CFHX temperature profile under influence of radiation.

CFHX temperature profile with radiation is depicted in figure 2.8. In this figure the solid line is the temperature profile with radiation. Such a temperature profile can originate from different initial temperature profiles without radiation. Due to unknown effect of radiation it is hard to obtain an effectiveness from such radiation temperature profile. What can be done is defining an upper- and lower limit of the effectiveness. In the best case scenario all heat of radiation is transferred to the high-pressure line and influences only the high-pressure line. This is indicated in the top graph of figure 2.8. Here the original temperature profile has a high effectiveness. This situation is most likely when the original temperature profile without radiation has a high effectiveness. This maximum effectiveness is defined as:

$$\epsilon_{max} = \frac{\Delta \dot{H}_{pL}}{\Delta \dot{H}_{max}}. \tag{2.12}$$

In the worst case scenario the radiation influences only the low-pressure line, as can be seen in the bottom graph of figure 2.8. This results in a low initial effectiveness. This situation is most likely when the original temperature profile without radiation has a low effectiveness, since then only little heat can be transferred to the high-pressure line. This minimum effectiveness is defined as:

$$\epsilon_{min} = \frac{\Delta \dot{H}_{pH}}{\Delta \dot{H}_{max}}. \tag{2.13}$$

The real effectiveness will be somewhere within this range. In the 'modeling result chapter' it will be indicated that it is hard to predict how the radiation distributes between the two pressure lines.

2.2.4 The error in the effectiveness and radiation

The CFHX of the final stage operates between 15 K and 8 K. From equation (2.9) it follows that operating at 99.8% effectiveness results in $T_{pL,out} = 14.984$ K and $T_{pH,out} = 8.022$ K. There is thus a small temperature differences between $T_{pH,in}$ and $T_{pL,out}$ of only 16 mK and a temperature difference between $T_{pL,in}$ and $T_{pH,out}$ of only 22 mK. For the accuracy of the measurement it is important to know the error in the effectiveness. During the experiments only temperatures are measured from which specific enthalpies are calculated. These specific enthalpies are then used in equation (2.9) to calculate the effectiveness. The error in temperature can be converted to error in specific enthalpy by the following relation:

$$c_p = \left(\frac{\partial h}{\partial T}\right)_p . \tag{2.14}$$

For small temperature differences c_p can be estimated as a constant resulting in the following expression:

$$\Delta h = c_p \Delta T. \tag{2.15}$$

The error in effectiveness of equation (2.9) is now given by equation (2.16), assuming that the error in all temperature readouts (ΔT) is the same:

$$\Delta\epsilon = \epsilon\sqrt{\left(\frac{\sqrt{\left[c_{p(pL,out)}\Delta T\right]^2 + \left[c_{p(pL,in)}\Delta T\right]^2}}{\Delta h_{pL}}\right)^2 + \left(\frac{\sqrt{\left[c_{p\,min(T_{pH,in})}\Delta T\right]^2 + \left[c_{p\,min(T_{pL,in})}\Delta T\right]^2}}{min\left[\Delta h_{max(pH)}, \Delta h_{max(pL)}\right]}\right)^2} . \tag{2.16}$$

The derivation of this formula is given in the appendix. Due to the high effectiveness the error in effectiveness needs to be < 0.2%. From equation (2.16) it follows that the error in temperature readout then needs to be < 5 mK. Cernox^{TM} CX-1050 sensors can deliver this accuracy [18]. The error in radiation, given by equation (2.11) is shown in equation (2.17). Also the derivation of this equation is given in the appendix.

$$\Delta\dot{Q}_{rad} = \dot{Q}_{rad}\sqrt{\left(\frac{\Delta\dot{m}}{\dot{m}}\right)^2 + \left(\frac{\sqrt{\left[(c_{p(pL,T_{pL,out})}\Delta T\right]^2 + \left[c_{p(pL,T_{pL,in})}\Delta T\right]^2 + \left[c_{p(pH,T_{pH,in})}\Delta T\right]^2 + \left[c_{p(pH,T_{pH,out})}\Delta T\right]^2}}{\Delta h_{pL} - \Delta h_{pH}}\right)^2} . \tag{2.17}$$

2.3 Joule-Thomson throttle

When gas flows through a Joule-Thomson throttle, the gas expands isenthalpically. Cooling during expansion can occur only when the Joule-Thomson coefficient μ_{JT}, which is given by equation (2.18), is positive. This happens when the temperature of

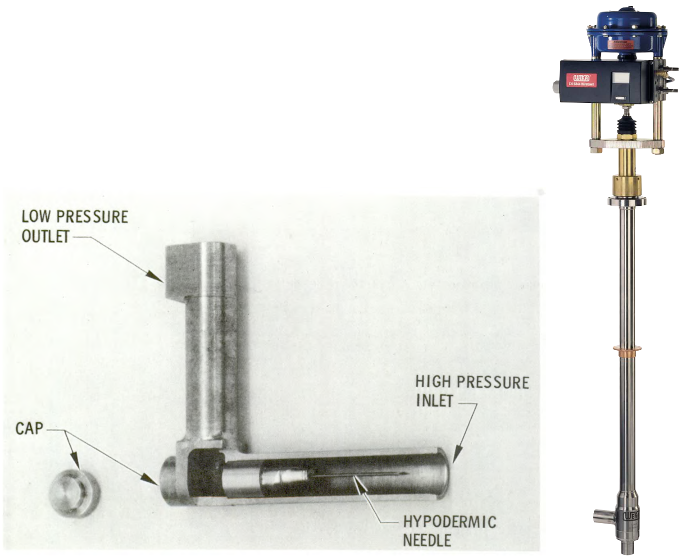

(a) (b)

Figure 2.9: (a): A needle restriction [20], (b): A tunable restriction [21].

the gas is below the so called inversion temperature. In case of helium this inversion temperature is 20 K.

$$\mu_{JT} = \left(\frac{\partial T}{\partial p}\right)_h \tag{2.18}$$

From an enthalpy balance the temperature after the restriction can be calculated. When helium gas expands from 14.32 bar @ 8 K to 7.46 bar, the temperature at the low-pressure side of the restriction will become 7.48 K. The gas does not liquefy during the JT expansion since the temperature after expansion stays above the critical temperature of helium, which is 5.19 K. There are different kinds of JT-throttles. For example a small hole or a capillary tube. A picture of a capillary tube restriction is given in figure 2.9(a). Another option is a tunable restriction. A tunable restriction has the advantage to reduce the cooling down time of the system. Initially at high temperature, the density is of the helium gas is low. This reduces the mass flow and thus energy transfer. Widening the restriction at the beginning of the cool down thus increases the mass flow and thus reduces the cooling down time. A picture of a tunable restriction is given in figure 2.9(b). This restriction only has a heat inleak of < 0.3 W from 300 to 20 K [19]. Another method to reduce the cool down time is to make a bypass around the restriction+CFHX, which closes when the final stage has cooled down.

2.4 Final stage HX

The final stage HX exchanges heat between the detector and the cold helium gas flow. The cold helium gas flow absorbs heat from the detector. This gas flow may heat up to a maximum of 8 K. The requirement for the final stage HX is to absorb 0.4 W of heat at 8 K. This means that the cooling power needs to be 0.4 W @ 8 K. The cooling power is a function of mass flow and specific enthalpy difference:

$$P_{cool} = \dot{m}\Delta h = \dot{m}\left[h_{HXout(T,p)} - h_{HXin(T,p)}\right] = \dot{m}\left[h_{HXout(8K,7.46bar)} - h_{HXin(7.48K,7.46bar)}\right] = 0.5W. \tag{2.19}$$

Here the specific enthalpy is dependent on the temperature and pressure. The mass flow is set to 100.03 mg/s. The helium flow enters the final stage HX with a temperature of 7.48 K and a pressure of 7.46 bar. The helium flow leaves the final stage HX with a temperature of 8 K and a pressure of 7.46 bar. Filling in the values results in a cooling power of 0.5 W. Here a margin of 25% has been taken into account for the cooling power. It is important that there is a good heat exchange in the final stage HX, so that the helium gas flow can adsorb all the heat coming from the detector. Considered here is a spiral gas channel in a copper block. An example of such a copper block can be seen in figure 5.2, where it is indicated as HX 1. Copper has a good thermal conductivity and can stabilize small temperature fluctuations. The channel needs a minimum length so enough heat can be transferred to the helium gas. A model of the final stage HX is treated in the modeling chapter.

Chapter 3

Modeling the CFHX

In the theory chapter the counterflow heat exchanger was introduced. In this chapter a model is described to predict the effectiveness of a tube-in-tube CFHX and a coiled finned tube CFHX. To start off, a CFHX is divided into N elements of length dx. Such a division is depicted in figure 3.1. The conduction in flow direction is neglected since these heat flows are much smaller than the difference in the enthalpy flow. For each cell an energy balance can be written. For the cells in the high- and low-pressure channels the energy balance is:

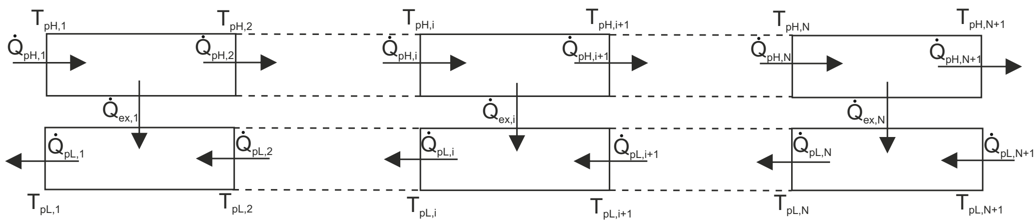

Figure 3.1: Schematic of a CFHX model.

$$\begin{aligned} \dot{Q}_{pH,i} - \dot{Q}_{pH,i+1} - \dot{Q}_{ex,i} &= 0 \\ \dot{Q}_{pL,i} - \dot{Q}_{pL,i+1} - \dot{Q}_{ex,i} &= 0. \end{aligned} \tag{3.1}$$

Here $\dot{Q}_{ex,i}$ is the heat exchanged from the high to the low-pressure channel and $\dot{Q}_{pH,i} - \dot{Q}_{pH,i+1}$ and $\dot{Q}_{pL,i} - \dot{Q}_{pL,i+1}$ are the energy differences between the left- and right boundary of the cell. $\dot{Q}_{pL,i}$ and $\dot{Q}_{pL,i+1}$ are evaluated at the boundary of the cell and $\dot{Q}_{ex,i}$ is evaluated at the center of the cell. The expressions of the two equations above can also be written in terms of temperature:

$$\begin{aligned} \dot{Q}_{pH,i} - \dot{Q}_{pH,i+1} &= \dot{m}c_{p_{pH,i}}\left(T_{pH,i} - T_{pH,i+1}\right) \\ \dot{Q}_{pL,i} - \dot{Q}_{pL,i+1} &= \dot{m}c_{p_{pL,i}}\left(T_{pL,i} - T_{pL,i+1}\right) \\ \dot{Q}_{ex,i} &= UA\left(\frac{T_{pH,i} + T_{pH,i+1}}{2} - \frac{T_{pL,i} + T_{pL,i+1}}{2}\right). \end{aligned} \tag{3.2}$$

Table 3.1: Explanation of the dimensions of a tube-in-tube CFHX.

Variable	Symbol
Inner tube, inner diameter	$D_{in,in}$
Inner tube, outer diameter	$D_{in,out}$
Outer tube, inner diameter	$D_{out,in}$
Outer tube, outer diameter	$D_{out,out}$

Here the temperatures are evaluated at the boundaries of the cell. For the-$\dot{Q}_{ex,i}$ term an average of the two boundaries temperatures is taken to evaluate the temperature in the center of the cell. $c_{p_{pH,i}}$ and $c_{p_{pL,i}}$ are both dependent on the temperature and pressure in the cell. U is the overall heat transfer coefficient and A is the area between the two channels, which are described in the next sections. Inserting equation (3.2) into equation (3.1) results in the following two coupled equations:

$$\begin{aligned}\dot{m}c_{p_{pH,i}}\left(T_{pH,i}-T_{pH,i+1}\right)-UA\left(\frac{T_{pH,i}+T_{pH,i+1}}{2}-\frac{T_{pL,i}+T_{pL,i+1}}{2}\right)&=0\\ \dot{m}c_{p_{pL,i}}\left(T_{pL,i}-T_{pL,i+1}\right)-UA\left(\frac{T_{pH,i}+T_{pH,i+1}}{2}-\frac{T_{pL,i}+T_{pL,i+1}}{2}\right)&=0.\end{aligned} \tag{3.3}$$

Giving two initial conditions of $T_{pH,1}$ and $T_{pL,N+1}$, the system of equations can be linearly solved with Matlab. For the properties of all the elements, for example c_p, an initial linear temperature profile is chosen. This profile is updated after solving the equations. After several iterations a steady temperature profile is obtained. The total thermal conductance term UA in the equations above varies for different kinds of CFHXs. In the next sections the UA term for different CFHXs is treated.

3.1 Tube-in-tube CFHX

Parameters used in the tube-in-tube CFHX calculations are described in table 3.1. The UA term in case of a tube-in-tube CFHX is given by equation (3.4):

$$UA=\frac{1}{\frac{1}{h_{pH}A_{pH}}+\frac{\ln\left(\frac{D_{in,out}}{D_{in,in}}\right)}{2\pi\lambda dx}+\frac{1}{h_{pL}A_{pL}}}. \tag{3.4}$$

The middle term in the denominator in equation (3.4) is the thermal resistance of the inner tube [10]. λ is the thermal conductivity of the wall material and h_{pH} and h_{pL} are the heat transfer coefficients of the high- and low-pressure channel respectively, which is given by equation (3.5):

$$h=\frac{Nu\lambda}{D_H}, \tag{3.5}$$

where D_H is the hydraulic diameter, Nu is the Nusselt number and λ is the thermal conductivity of the gas. The hydraulic diameter is defined by:

$$D_H=\frac{4A}{P}, \tag{3.6}$$

where A is the cross sectional area and P is the perimeter of the cross-section. In case of a round tube $D_H = D_{in,in}$ and in case of an annulus $D_H = D_{out,in} - D_{in,out}$. Nu is the ratio of convective to conductive heat transfer across a boundary. For round channels Nu is defined by [22]:

$$\begin{aligned} Nu_C &= 3.657 && for \quad Re < 2300 \\ Nu_C &= \frac{(f/8)(Re-1000)Pr}{1+12.7(f/8)^{1/2}\left(Pr^{2/3}-1\right)} && for \quad Re > 2300, \end{aligned} \tag{3.7}$$

where the parameters f, Re and Pr are described below. For $2300 < Re < 4000$ the flow is in the transition regime. This is a grey area where the flow is between laminar and turbulent. For annular channels Nu is defined by [23]:

$$\begin{aligned} Nu_A &= 3.66 + \left[4 - \frac{0.102}{\left(\frac{D_{in,out}}{D_{out,in}}\right)+0.2}\right]\left(\frac{D_{in,out}}{D_{out,in}}\right)^{0.04} && for \quad Re < 2300 \\ Nu_A &= Nu_C 0.86\left(\frac{D_{in,out}}{D_{out,in}}\right)^{-0.16} && for \quad Re > 2300 \end{aligned} \tag{3.8}$$

Re is the Reynolds number defined by:

$$Re = \frac{\dot{m}D_H}{\mu A}. \tag{3.9}$$

Re is a dimensionless number that gives a measure of the ratio of inertial forces to viscous forces. At $Re < 2300$ the flow is laminar and at $Re > 2300$ the flow becomes turbulent. Furthermore, in equation (3.9) A is the cross sectional area of the gas channel and μ is the dynamic viscosity of the gas. In equation (3.7) Pr is the Prandtl number defined by:

$$Pr = \frac{c_p \mu}{\lambda}. \tag{3.10}$$

Pr is a dimensionless number and gives the ratio of momentum diffusivity to thermal diffusivity. Furthermore, λ in equation (3.10) is the thermal conductivity of the gas. In equation (3.7) f is the Darcy friction factor. For circular ducts f is defined by [10]:

$$\begin{aligned} f_C &= \frac{64}{Re} && for \quad Re < 2300 \\ f_C &= 0.316Re^{-0.25} && for \quad 2300 < Re < 20000 \\ f_C &= 0.184Re^{-0.20} && for \quad Re > 20000. \end{aligned} \tag{3.11}$$

and for annular ducts f is defined by equation (3.12) [22]:

$$\begin{aligned} f_A &= \frac{64\,(1-r^*)^2}{Re\left(1+r^{*2}-2r_m^{*2}\right)} \quad for \quad Re < 2300 \quad with \\ & r_m = \left(\frac{1-r^{*2}}{2\ln\left(1/r^*\right)}\right)^{1/2}, r^* = \frac{D_{in,out}}{D_{out,in}}. \end{aligned} \tag{3.12}$$

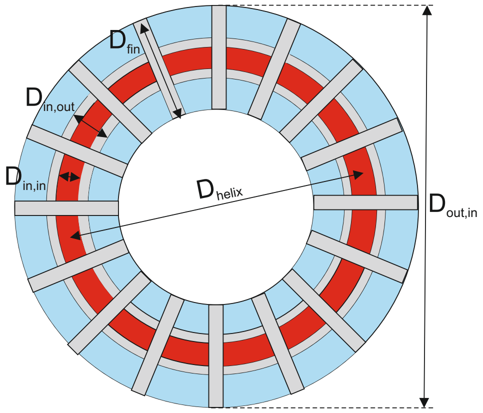

Figure 3.2: Schematic of the coiled finned tube CFHX.

For $Re > 2300$ equation (3.11) for the circular duct can be used [22]. The pressure drop is given by the Darcy-Weisbach equation [10]:

$$\Delta p = f \frac{L}{D_H} \frac{1}{2} \frac{\dot{m}^2}{\rho A^2}, \tag{3.13}$$

where L is the length of the channel, ρ is the density of the gas and A is the cross-sectional area of the gas flow.

3.2 Coiled finned tube CFHX

A schematic of the coiled finned tube CFHX is given in figure 3.2. Here the red channel is the high-pressure line which lies inside the finned tube and is coiled around the mandrel. The blue channel is the low-pressure line which lies around the finned tube, between the inner- and outer mandrel.

In case of the coiled finned tube CFHX the UA term in equation (3.3) is replaced by $\epsilon C_{min}(C = \dot{m}c_p)$ [24], see also equation (3.14). This method is called the Number of Transfer Units (N_{tu}) Method and is used when the inlet- and outlet temperatures are not specified.

$$\begin{aligned} \dot{m}c_{p_{pH,i}}\left(T_{pH,i} - T_{pH,i+1}\right) - \epsilon C_{min}\left(\frac{T_{pH,i} + T_{pH,i+1}}{2} - \frac{T_{pL,i} + T_{pL,i+1}}{2}\right) &= 0 \\ \dot{m}c_{p_{pL,i}}\left(T_{pL,i} - T_{pL,i+1}\right) - \epsilon C_{min}\left(\frac{T_{pH,i} + T_{pH,i+1}}{2} - \frac{T_{pL,i} + T_{pL,i+1}}{2}\right) &= 0. \end{aligned} \tag{3.14}$$

Here ϵ is the effectiveness and C_{min} is the minimum of the heat capacities of the high and low-pressure gas. ϵ can be expressed as [24]:

$$\epsilon = 1 - \exp\left\{-\frac{[1 - \exp(-C_R N_{tu})]}{C_R}\right\}. \tag{3.15}$$

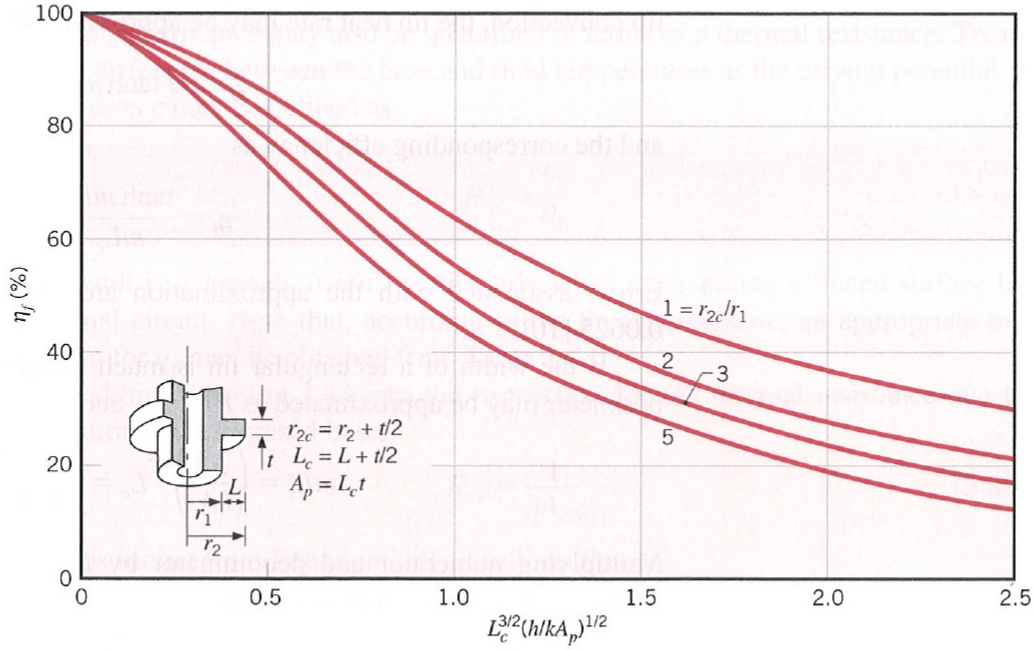

Figure 3.3: Adiabatic fin effectiveness for a finned tube [26].

This relation is valid for a coiled finned tube CFHX since there is crossflow and C_{min} is mixed and C_{max} is unmixed (defined to a flow passage). In equation (3.15) C_R is the ratio between the minimum and maximum capacity rate ($C_R = \frac{C_{min}}{C_{max}}$) and N_{tu} is the dimensionless number of transfer units defined by equation (3.16):

$$N_{tu} = \frac{UA}{C_{min}} \tag{3.16}$$

Here the UA term is slightly different than in the tube-in-tube CFHX [16]:

$$UA = \frac{1}{\frac{1}{h_{pH}A_{pH}} + \frac{\ln\left(\frac{D_{in,out}}{D_{in,in}}\right)}{2\pi\lambda dx} + \frac{1}{\eta_0 h_{pL} A_{pL}}}. \tag{3.17}$$

In this equation η_0 is the fin efficiency. Temperature gradients along the fins extending into the gas reduce the temperature effectiveness of the surface, therefore $\eta_0 < 1$. η_0 is a weighted average of the 100 percent effectiveness of the prime surface and the less than 100 percent effectiveness of the fin surface η_f. Therefore the fin efficiency is defined as:

$$\eta_0 = 1 - \frac{A_f}{A_{pL}}\left(1 - \eta_f\right), \tag{3.18}$$

where A_f is the area of the fin, A_{pL} is the total area of the fins plus tube in the part of the CFHX that is considered and η_f is the adiabatic fin efficiency given by figure 3.3 [25].

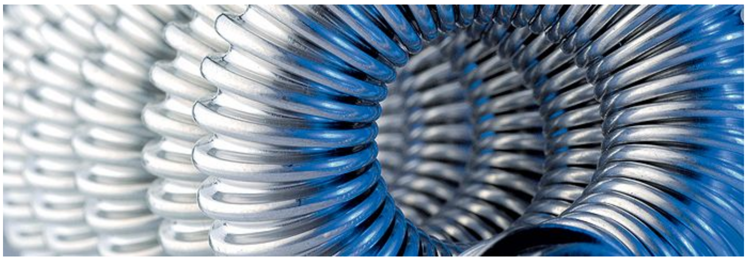

Figure 3.4: Corrugated tube [27].

In figure 3.3 k is the thermal conductivity of the fin material evaluated at the mean temperature between the streams. h_{pL} and h_{pH} are also different for a coiled finned tube CFHX compared to the tube-in-tube CFHX [16]:

$$\begin{aligned} h_{pH} &= 0.023\frac{1}{D_{in,in}}\lambda Re^{0.8}Pr^{1/3}\left(1+3.5\frac{D_{in,in}}{D_{helix}}\right) \\ h_{pL} &= 0.26\frac{1}{D_{annulus}}\lambda Re^{0.6}Pr^{1/3}, \end{aligned} \tag{3.19}$$

where $D_{annulus}$ is given by the sum of the hydraulic diameter of the two annuli of the low-pressure stream since the gas flows at both sides of the finned tube, see also figure 3.2. The pressure drop for the coiled finned tube CFHX is given by equation (3.20):

$$\begin{aligned} \Delta p_{pH} &= f_{pH}\frac{l}{D_H}\frac{1}{2}\frac{\dot{m}^2}{\rho A^2} \\ \Delta p_{pL} &= f_{pL}N_L\frac{1}{2}\frac{\dot{m}^2}{\rho A^2}, \end{aligned} \tag{3.20}$$

where N_L is the number of rows of tubes. The friction factor is given by equation (3.21) [16, 24]:

$$f_{pH} = \frac{0.184}{Re^{0.2}}\left(1+3.5\frac{D_{in,in}}{D_{helix}}\right). \tag{3.21}$$

f_{pL} is also given by equation (3.12) and for $Re > 2300$ the equations from equation (3.11) are used.

Instead of finned tube also corrugated tube is used in coiled finned tube heat exchangers. The fins of the corrugated tube are hollow and often larger, resulting in a better flexibility of the tube. A picture of a corrugated tube is given in figure 3.4. The model for the finned tube can also be applied for the corrugated tube taking the extra surface area inside the high-pressure line into account. A coiled corrugated tube CFHX is analyzed in the modeling result section of this thesis.

3.3 Modeling radiation influence onto a CFHX

When radiation falls onto the low-pressure line of the CFHX an additional radiation term $\dot{Q}_{rad}$ enters the energy balance equations:

$$\begin{aligned}\dot{Q}_{pH,i} - \dot{Q}_{pH,i+1} - \dot{Q}_{ex,i} &= 0\\ \dot{Q}_{pL,i} - \dot{Q}_{pL,i+1} - \dot{Q}_{ex,i} - \dot{Q}_{rad,i} &= 0.\end{aligned} \tag{3.22}$$

This new situation is depicted in figure 3.5.

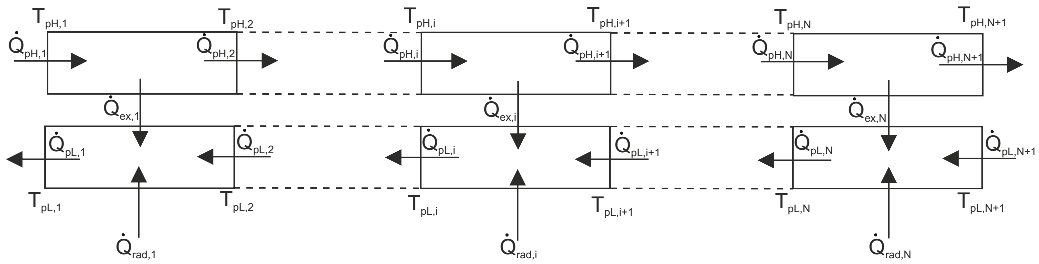

Figure 3.5: Schematic of a CFHX with radiation.

Here the radiation falls onto the center of the cell. Writing equation (3.22) in terms of temperature results in:

$$\begin{aligned}&\dot{m}c_{p\,pH,i}\left(T_{pH,i} - T_{pH,i+1}\right) - UA\left(\frac{T_{pH,i} + T_{pH,i+1}}{2} - \frac{T_{pL,i} + T_{pL,i+1}}{2}\right) = 0\\ &\dot{m}c_{p\,pL,i}\left(T_{pL,i} - T_{pL,i+1}\right) - UA\left(\frac{T_{pH,i} + T_{pH,i+1}}{2} - \frac{T_{pL,i} + T_{pL,i+1}}{2}\right) - \frac{\sigma\left(T_{amb}^4 - \left(\frac{T_{pL,i}+T_{pL,i+1}}{2}\right)^4\right)}{\frac{1-\varepsilon_1}{\varepsilon_1 A_1} + \frac{1}{A_1} + \frac{1-\varepsilon_2}{\varepsilon_2 A_2}} = 0.\end{aligned} \tag{3.23}$$

Due to the non-linearity of the radiation term (T^4), the system of equations cannot be linearly solved anymore, but has to be solved with the fsolve function of Matlab.

3.4 Modeling the CFHX without flow

To get a better insight into the heat loads working onto the CFHX it is also good to measure the temperature profile without flow.

3.4.1 Without radiation

When there is no flow inside the CFHX and no radiation onto the CFHX, the temperature profile is only determined by the conduction through the CFHX material. A schematic of this situation is given in figure 3.6. For every cell an energy conservation equation can be written. This equation is given by:

$$\dot{Q}_{con,i} - \dot{Q}_{con,i+1} = 0 \tag{3.24}$$

In terms of temperature equation (3.24) becomes:

$$\frac{A_i\lambda_i}{dx_i}(T_i - T_{i+1}) - \frac{A_{i+1}\lambda_{i+1}}{dx_{i+1}}(T_{i+1} - T_{i+2}) = 0. \tag{3.25}$$

This system of equations can be linearly solved with Matlab. Note that the conductivity through the stainless steel and helium gas has to be taken into account.

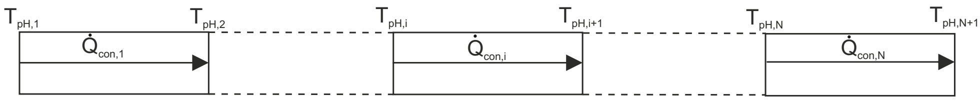

Figure 3.6: Schematic model of conduction.

3.4.2 With radiation

When radiation falls onto a CFHX without flow, the radiation term $\dot{Q}_{rad}$ enters the energy balance equation:

$$\dot{Q}_{con,i} - \dot{Q}_{con,i+1} + \dot{Q}_{rad,i} = 0 \tag{3.26}$$

Here the radiation falls onto the boundaries of the cell, which can also be seen in figure 3.7. In terms of temperature equation (3.26) becomes:

$$\frac{A_i\lambda_i}{dx_i}(T_i - T_{i+1}) - \frac{A_{i+1}\lambda_{i+1}}{dx_{i+1}}(T_{i+1} - T_{i+2}) + \frac{\sigma\left(T_{amb}^4 - T_i^4\right)}{\frac{1-\varepsilon_1}{\varepsilon_1 A_1} + \frac{1}{A_1} + \frac{1-\varepsilon_2}{\varepsilon_2 A_2}} = 0 \tag{3.27}$$

Due to the non-linearity of the radiation term (T^4), the system of equations cannot be linearly solved anymore, but has to be solved with the fsolve function of Matlab.

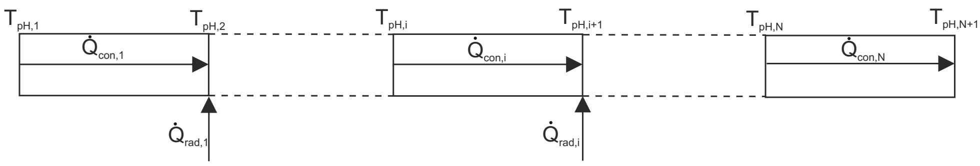

Figure 3.7: Schematic of the conduction model with radiation.

3.5 Final stage HX

The final stage HX can be modeled as a CFHX with one side of the CFHX kept at 8 K. A schematic of the final stage HX is given in figure 3.8. The final stage HX is modeled as a square spiraling copper channel, in which the helium gas flows. The hydraulic diameter for square channels is given by $D_H = L_{side}$, where L_{side} is the length of one of the sides of the square channel. The temperature profile in the final stage HX can be obtained by setting T_{pL} of equation (3.3) to 8 K. Due to the square cross section the Nusselt number will change to: $Nu = 3$ for $Re < 2300$ [22] and the friction factor will change to $f_{Sq} = \frac{56.8}{Re}$ for $Re < 2300$. For $Re > 2300$ equation (3.7) and equation (3.11) apply for Nu and f respectively.

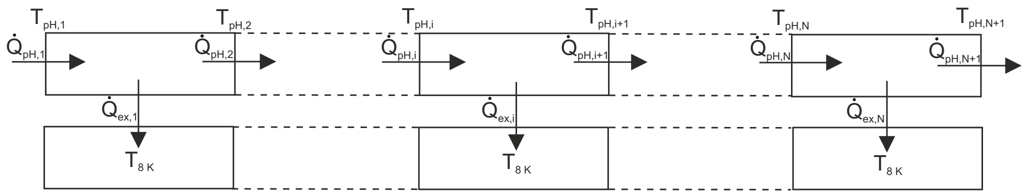

Figure 3.8: Schematic of the final stage HX.

Chapter 4

Final stage characterization setup

4.1 Introduction

The final stage needs to be characterized. To do this a characterization setup has been designed. A schematic of this setup is given in figure 4.1. The final stage is situated in the middle of the setup, inside radiation shield 2. Since the neon, hydrogen and upper stages of the helium stage are not yet fabricated, pre-cooling to 15 K is done by a two stage GM-cooler, see figure 4.3. The first- and second stage of the GM-cooler are connected to heat exchangers (HX 1 and HX 2). These heat exchangers allow the GM-cooler to extract heat from the incoming helium gas. These HXs are fabricated from copper blocks with grooves machined into these which serve as spiral gas channels. The outlet temperature of HX 1 and HX 2 will be equal to the GM-cooler stage temperature T_1 and T_2, respectively. In the 'modeling results chapter' this assumption is validated. Between ambient and HX 1 and between HX 1 and HX 2 two CFHXs are placed (CFHX 1 and CFHX 2). These CFHXs also cool down the incoming gas. To lower the parasitic heat losses onto the final stage, two radiation shields are placed into the setup. These radiation shields are closed thin copper cylinders. The first radiation shield is connected to the first stage of the GM-cooler and the second radiation shield is connected to the second stage of the GM-cooler. To further reduce the parastics, the first stage radiation shield is wrapped with MLI. Also the wiring is thermally anchored to the radiation shields.

4.2 Analysis

In this section the final stage characterization setup is analyzed. Before the analysis starts some concepts have to be introduced.

4.2.1 GM cooler performance

It is important to know how much cooling power is available at both stages of the GM-cooler as function of the temperatures of both stages. This data can be obtained from a load curve measurement. The other way around: from a load curve measurement the

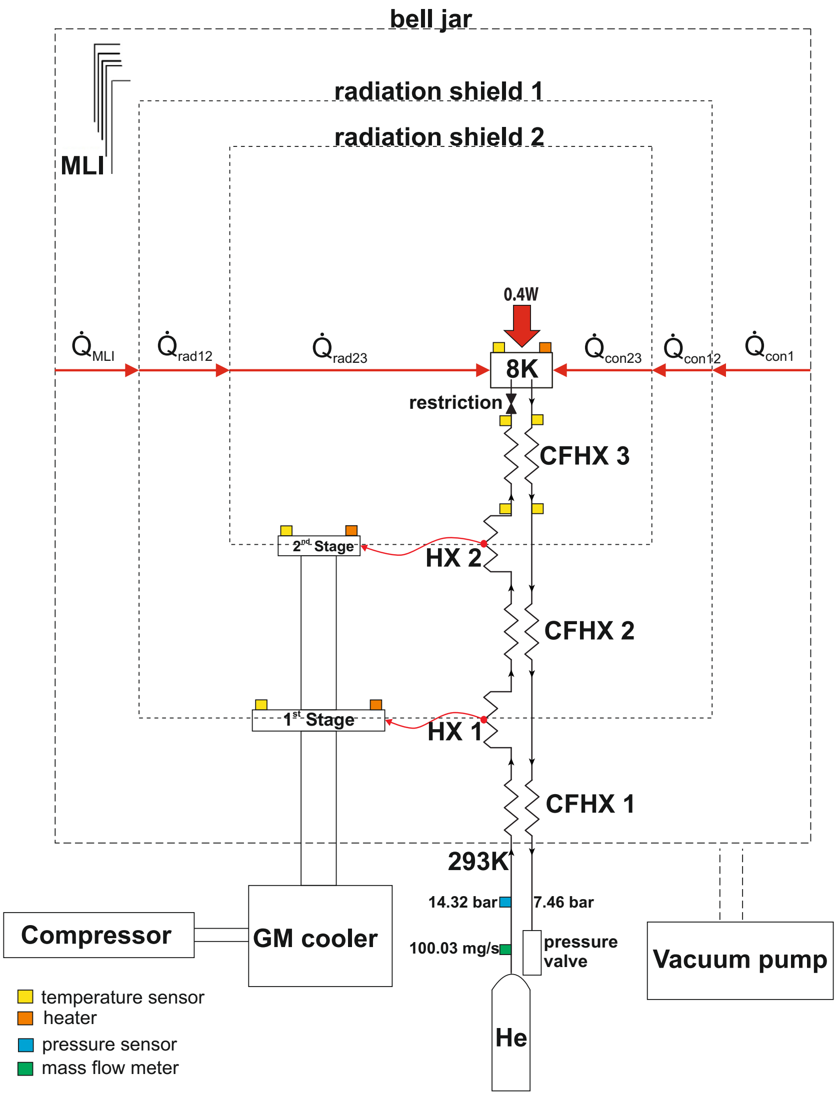

Figure 4.1: Schematic of the final stage characterization setup.

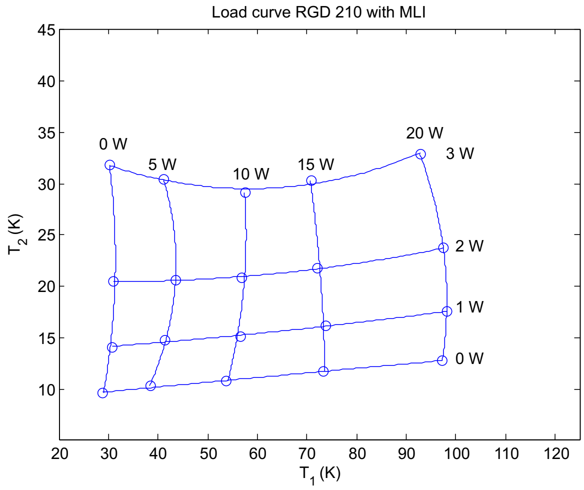

Figure 4.2: The load curve of the GM-cooler.

temperature of the GM-cooler stages can be determined as function of the heat load. This is summarized in equation (4.1) for the first stage GM-cooler.

$$\dot{Q}_1 (T_1, T_2) \Leftrightarrow T_1 \left(\dot{Q}_1, \dot{Q}_2\right) \tag{4.1}$$

In this equation Q_1 is the total heat load on the first stage. In a load curve measurement parasitics on the GM-cooler are minimized and a known heat load is applied on both stages with a heater and the temperatures are measured. The measured load curve from the GM-cooler used in the final stage characterization setup is given in figure 4.2.

4.2.2 System behavior

The final stage characterization setup is a complex coupled system and a lot of parameters influence the helium inlet temperature of the final stage. First there are the parasitic heat loads. The parasitic heat loads are shown as red arrows in figure 4.1. These heat loads are conduction through the wiring and support ($\dot{Q}_{con}$), the radiation between the shields ($\dot{Q}_{rad}$) and the heat load through the MLI ($\dot{Q}_{MLI}$).

Another parameter is the cooling power of the GM-stages. The higher the cooling capacity of the GM-cooler, the more heat can be taken away by it. When the GM-cooling power is high, CFHX 1 and CFHX 2 can be made less effective. The low effectiveness of the CFHX is than compensated by the high cooling power of the GM-cooler. The amount of heat taken away from the helium by e.g. the first stage GM-cooler is given by:

$$\begin{aligned}\dot{Q}_{He1} &= \dot{m}\left[h\left(T_{HX1in}\right) - h\left(T_{HX1out}\right)\right] \\ &= \dot{m}\left[h\left(T_{HX1in}\right) - h\left(T_1\right)\right].\end{aligned} \tag{4.2}$$

Here it is assumed that the outcoming temperature of HX 1 (T_{HX1out}) is equal to the GM-cooler temperature (T_1), so $T_{HX1out} = T_1$. In the 'modeling results chapter' this

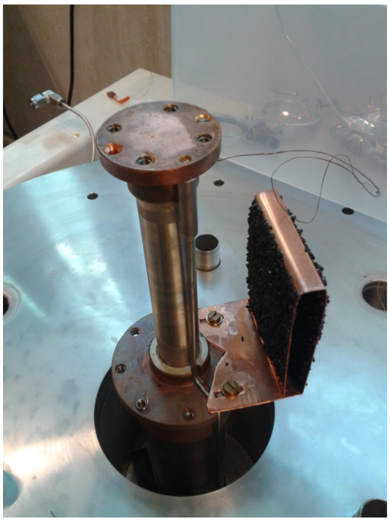

Figure 4.3: Picture of the GM-cooler.

assumption is validated. An overview of the different temperature levels in the final stage characterization setup is schematically given in figure 4.4.

The parameters $\dot{Q}_{He1}$ and $\dot{Q}_1$ and the parasitic heat loads can be combined in a heat flow model. For the 1st- and 2nd stage of the GM cooler the heat flow energy balances are:

$$\begin{aligned} \dot{Q}_1 &= \dot{Q}_{He1} + \dot{Q}_{MLI} + \dot{Q}_{con1} - \dot{Q}_{rad12} - \dot{Q}_{con12} \\ \dot{Q}_2 &= \dot{Q}_{He2} - \dot{Q}_{rad23} - \dot{Q}_{con23} + \dot{Q}_{rad12} + \dot{Q}_{con12}. \end{aligned} \tag{4.3}$$

These equations are coupled since both are dependent on T_1 and T_2. This is also illustrated in the equations below:

$$\begin{aligned} \dot{Q}_1(T_1, T_2) &= \dot{Q}_{He1}(T_1, T_{HX1in}) + \dot{Q}_{MLI}(T_{amb}, T_1) + \dot{Q}_{con1}(T_{amb}, T_1) - \dot{Q}_{rad12}(T_1, T_2) - \dot{Q}_{con12}(T_1, T_2) \\ \dot{Q}_2(T_1, T_2) &= \dot{Q}_{He2}(T_2, T_{HX2in}) - \dot{Q}_{rad23}(T_2, T_3) - \dot{Q}_{con23}(T_2, T_3) + \dot{Q}_{rad12}(T_1, T_2) + \dot{Q}_{con12}(T_1, T_2). \end{aligned} \tag{4.4}$$

Here T_3 (=8 K) is the temperature of the final stage, T_2 (=15 K) is the temperature of the second stage and T_{amb} (=293 K) is the ambient temperature. The unknowns from this equation are T_1 and T_{HX1in}. Solving this set of equations is referred to as the HX model.

To solve the system of equations first some dimensions and properties of the system need to be defined. For example the areas of the radiation shields, which are used in the radiation equation. T_1 and T_{HX1in} depend on the effectiveness of CFHX 1. An effectiveness of CFHX 1 has to be chosen. Since T_1 and T_{HX1in} are initially not known an iteration method needs to be used. An initial temperature of T_1 is guessed. By using the CFHX model T_{HX1in} can be calculated. Using then T_{HX1in} in the HX model of equation (4.4) results in a new value of T_1. This new value of T_1 is then used again in the CFHX model. This process is repeated until the value of T_1 converges. This

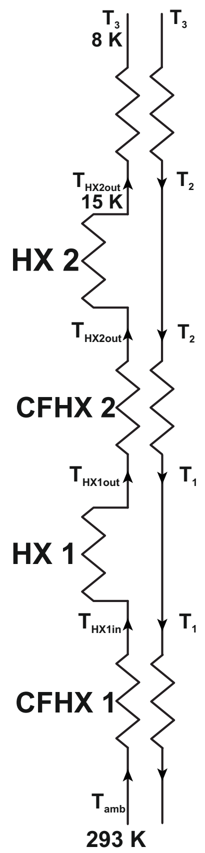

Figure 4.4: Temperatures of the final stage characterization setup.

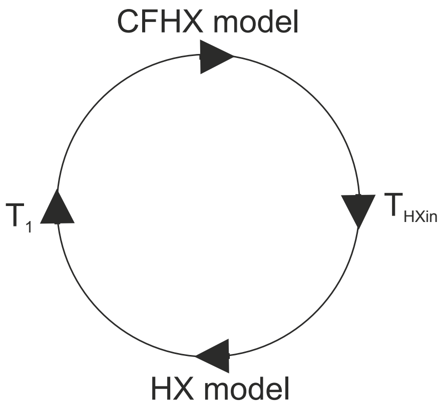

Figure 4.5: Schematic of the iteration.

process is schematically depicted in figure 4.5. Using T_1 in the CFHX model is the worst case scenario since CFHX 2 will not be 100% effective.

The only variable left is the effectiveness of CFHX 2. From equation (4.2) T_{HX2in} can be calculated. From this value in addition with T_1 and T_2 the effectiveness of CFHX 2 can be calculated. Different combinations of effectiveness of CHFX 1 and CFHX 2 can be used to obtain a T_2 of 15 K.

4.3 Mass flow through the restriction

For different type of restrictions different mass flow formulas apply. For the restrictions of a hole/small tube a general formula can be derived. This formula is given by:

$$\dot{m}(T) = \frac{D_H^2 A}{2CL} \int_{pL}^{pH} \frac{\rho(p,T)}{\mu(p,T)} dp, \tag{4.5}$$

where L is the length and A is the cross-sectional area of the restriction. Note that the ρ and μ need to be integrated over the pressure difference. This formula is derived from equation (3.13), where for the friction factor the following general friction factor expression was substituted [10]:

$$f = \frac{C}{Re} = \frac{C\mu A}{\dot{m} D_H}, \tag{4.6}$$

where C is a constant depending on the geometry of the restriction.

For circular restrictions $C = 16$ [10] and equation (4.5) simplifies to:

$$\dot{m}(T) = \frac{\pi D^4}{128L} \int_{pL}^{pH} \frac{\rho(p,T)}{\mu(p,T)} dp, \tag{4.7}$$

where D is the diameter of the circular restriction.

Manufacturers of tunable restrictions choose to publish a C_v (American units) or a K_v (SI units) flow coefficient to describe the flow/pressure loss characteristics of a restriction in a standardized manner. K_v is the rate of flow of cold water in cubic meter per hour at a pressure drop of one kilogram per square centimeter across the valve. For subcritical pressure drops, i.e. if $\Delta p < \frac{p_{in}}{2}$, the K_v value for gasses is given by equation (4.8) [28]:

$$K_v = \frac{W}{514}\sqrt{\frac{T_{in}}{\rho_N \Delta p \cdot p_{out}}}, \tag{4.8}$$

where Δp is the pressure drop over the restriction and W is the mass flow rate per hour and ρ_N is the gas density in standard condition (T = 273 K, p = 1013 mbar). Filling in the values of the final stage restriction results in a K_v value of 0.00065 m^3/h.

4.4 Experimental aspects

It is important to note that there are two helium cycles in the final stage characterization setup. The first helium cycle is the GM cold head (Leybold RGD210) which is connected to a compressor (Leybold, RW2) that compresses helium gas which than expands in the GM to deliver cooling power. This helium flow thus only flow through the GM-cooler and is disconnected from the rest of the experimental setup. The second helium cycle is the helium flow through the experimental setup, thus the flow through the CFHXs, JT-throttle and final stage HX. Helium for the final stage characterization setup is provided and regulated from a helium bottle. One helium bottle can deliver a 100 mg/s mass flow rate for around five hours before it empties. A pressure relief valve is placed at the flow outlet to set the pressure of the low-pressure line at 7.46 bar. The helium coming out of the pressure relief valve is captured and send into a helium recovery system. Temperature sensors are placed on both stages of the GM-cooler to measure the inlet temperatures. Also temperature sensors are place on the in- and outlets of CFHX 3 to measure its effectiveness. Finally a temperature sensor is placed on the final stage HX to measure the cooling temperature. Heaters are placed on both stages of the GM-cooler to regulate the temperature when necessary. Especially the temperature control of the second stage is important since this temperature needs to be exactly 15 K. Also a heater is mounted onto the final stage HX to apply the 0.4 W heat load. The temperature sensors are connected with manganin wire and the heaters are connected with copper wire. Also a pressure sensor and mass flow meter is placed in the setup, see figure 4.1. The whole setup is placed inside a bell jar which can be pumped to vacuum. This vacuum minimizes the convective heat transfer.

Chapter 5

CFHX effectiveness characterization setup

Due to a limited time span of the research the large final stage characterization setup has not yet been built. Instead a smaller setup has been built to test the effectiveness of a CFHX: the CFHX effectiveness characterization setup. Modeling results can be compared with measurements from the effectiveness characterization setup for validation. A schematic of the effectiveness characterization setup is given in figure 5.1.

A 3.02 m tube-in-tube CFHX, which was already available from a previous setup, has been tested in this setup. Results from this measurement can be extrapolated for the CFHX in the final stage: a 99.8% effective 17.16 m long length tube-in-tube CFHX. In the effectiveness characterization setup, helium gas at room temperature is forced to flow into a CFHX. After flowing through the CFHX the gas is cooled down by the first stage heat exchanger (HX 1), which is connected to the first stage of the GM-cooler. After cooling, the gas flows back through the CFHX and cools the incoming gas stream. In this way a temperature difference is established in the CFHX between ambient and the cryogenic temperature of the GM-cooler. After a specific time the temperature profile in the CFHX will reach equilibrium. At high mass flow this equilibrium sets in within the hour, but for lower mass flows it can take longer. By measuring the in- and outlet temperatures of the CFHX the effectiveness can be obtained from equation (2.7).

5.1 Experimental aspects

The effectiveness characterization setup also has two helium flow cycles. The first cycle is the GM-cooler which is connected to a helium compressor. The second cycle is the helium flow through the CFHX. A pressure relief valve is placed at the flow outlet to have a certain amount of pressure in the CFHX. Helium flow is provided and regulated from a helium bottle. A mass flow meter (Bronkhorst F-111AC) is used to measure the mass flow. The helium coming out of the pressure relief valve is captured and sent into a helium recovery system. A pressure sensor (PTX 1400) is used to measure the pressure. Temperature sensors are placed at the in- and outlets of the CFHX to measure the effectiveness of the CFHX. The accuracy of these sensors is given in table 5.1.

Also a temperature sensor and heater (22 Ω) is placed onto HX 1 to measure and control its temperature. Measuring the temperature of HX 1 can give extra information about the measurement, for example the radiation heat inleak. An AIRPAX sensor is

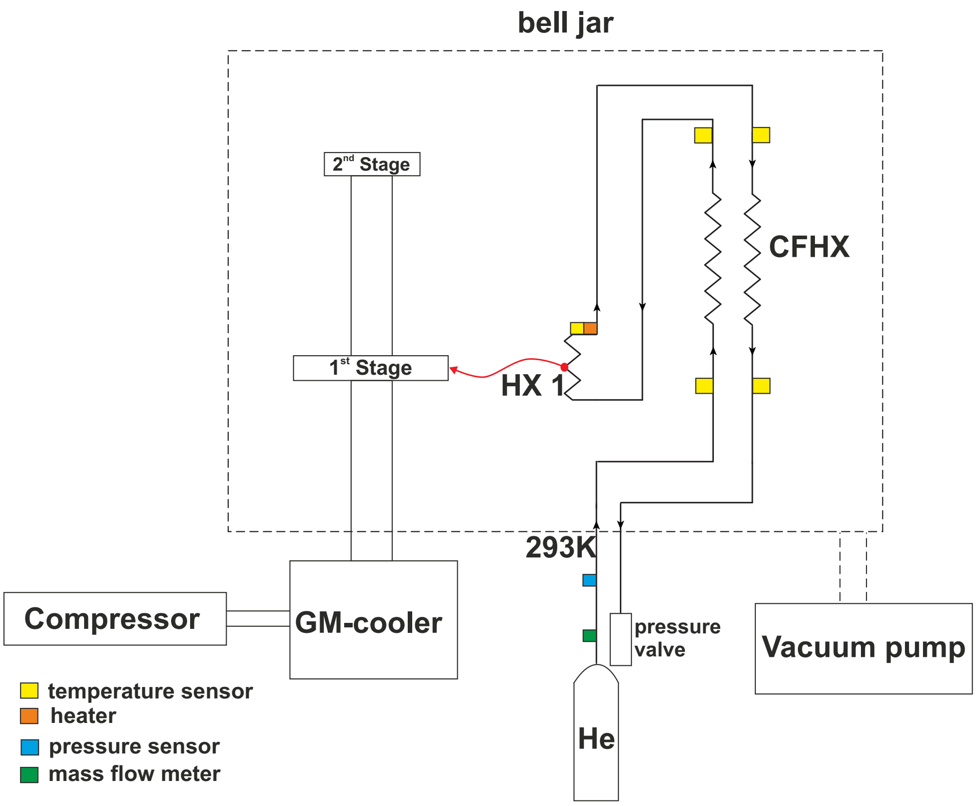

Figure 5.1: Schematic of the CFHX effectiveness characterization setup.

Table 5.1: Accuracy of the sensors used in the CFHX effectiveness characterization setup [18, 29].

Variable	Sensor	Accuracy
$T_{pL,in}$ $T_{pL,out}$ $T_{pH,in}$	DT-670A1-SD	± 0.25 K for T ≤ 100 K, ± 0.5 K for T > 100 K
$T_{pH,out}$	DT471-SD	± 1.5 K for T ≤ 100 K, 1.5% of temp for T > 100 K
$\dot{m}$	Bronkhorst F-111 AC	0.35%

placed in series with the heater as protection in case of overheating. The temperature sensors are connected with manganin wires and the heaters are connected with copper wires. The whole setup is placed inside a bell jar which can be pumped to vacuum with a vacuum pump (Pfeiffer Vacuum TSH 261). This vacuum minimizes the convective heat transfer. A picture of the setup with the bell jar removed is given in figure 5.2.
In this figure HX 1 is the copper block mounted on the first stage of the GM-cooler. Inside this copper block spiral channels are machined. Furthermore, the spiraling stain-

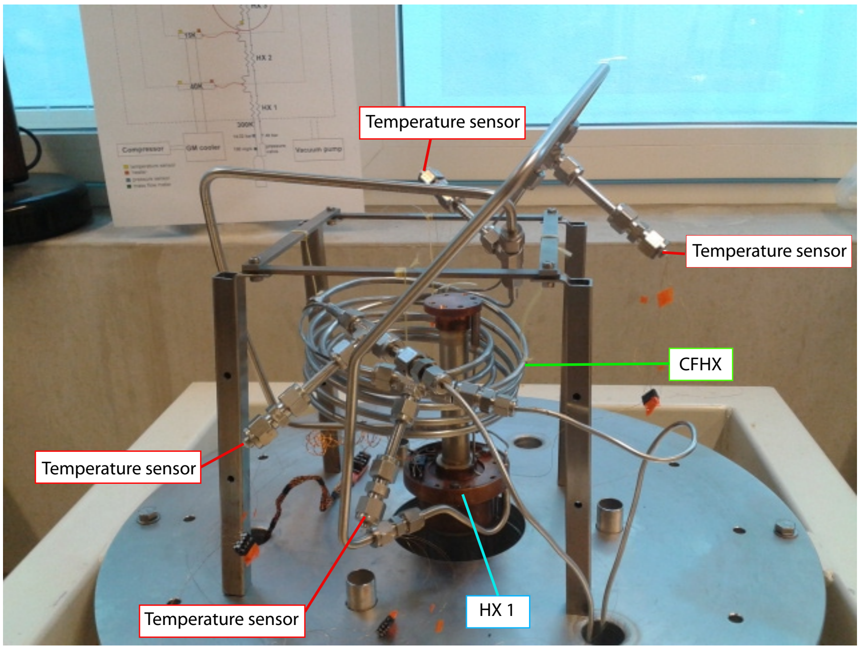

Figure 5.2: Picture of the CFHX effectiveness characterization setup.

less steel tubing is the CFHX. The temperature sensors at the in- and outlets of the CFHX are placed in so called 'pipe tees' and are also depicted in figure 5.2. This part is called the 'temperature measurement device'. Detailed pictures of the temperature measurement device are given in figure 5.3.

The device consists out of tubing with a temperature sensor placed inside. The wiring goes outside the tubing through a small 1 mm hole drilled into the plug. The hole is then filled with Torr Seal (circled with red). This part is successfully tested to withstand a pressure of 15 bar without leaking. A layer of insulating Kapton is wrapped inside the tubing so the temperature sensor (indicated by the green square) is insulated from the wall of the tubing. The device takes care that the gas temperature is measured inside the gas stream. This makes the temperature readout more accurate. Placing the temperature on the outside of the tubing might give an incorrect value due to a temperature gradient over the wall of the tubing. To lower the radiation heat inleak, the setup is wrapped in with MLI, see also figure 5.4.

First the MLI is wrapped about two times around the tubing. After this the whole setup is shielded with large MLI sheets. To prevent heat inleak through conduction, the CFHX and the tubing around the CFHX cannot touch any other part of the setup. The dimensions and properties of the setup are given in table 5.2. Note that there is a small narrowing of the tubing just before HX 1. To prevent clogging of the system

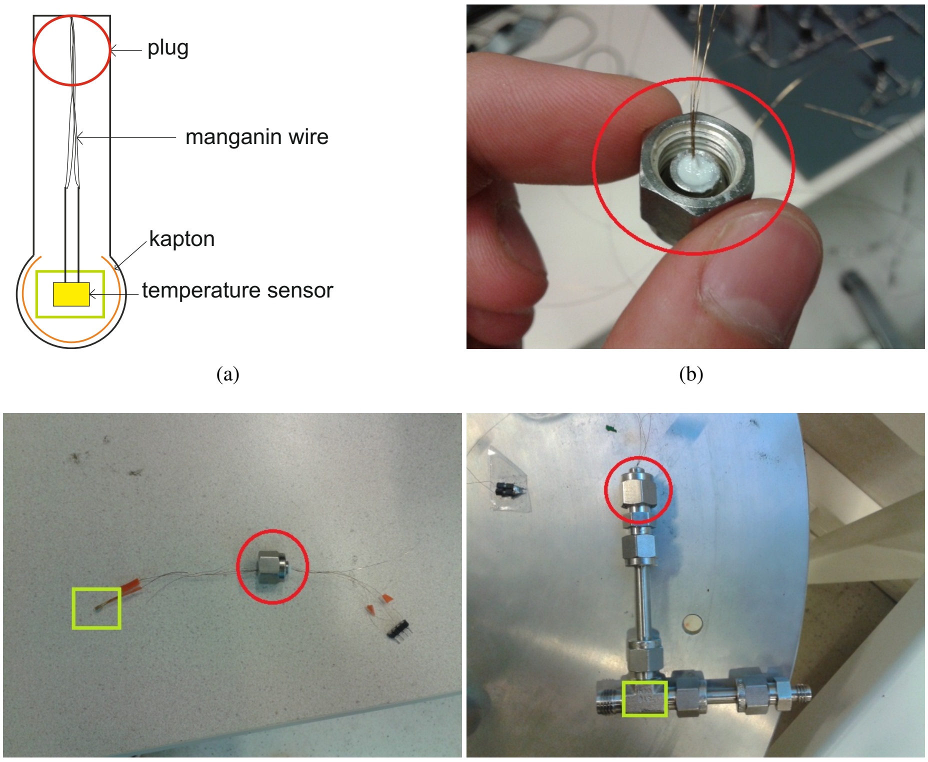

(a) (b) (c) (d)

Figure 5.3: The temperature measurement device. (a): Schematic cross section of the temperature measurement device. (b): Fabricated plug. (c): Fabricated plug connected to the temperature sensor and socket connectors. (d): Fabricated plug inserted into tubing.

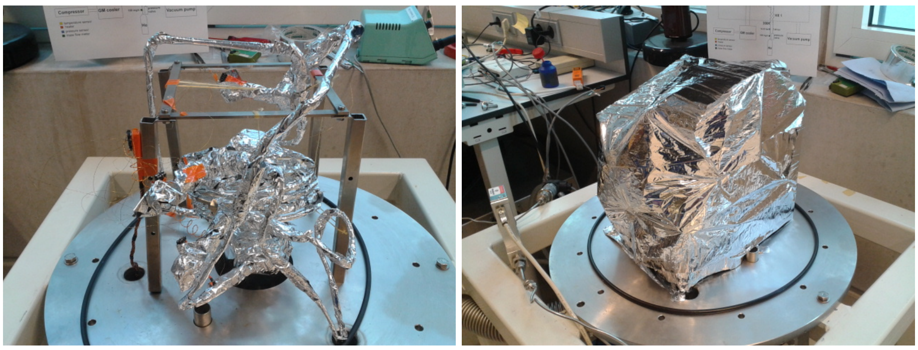

(a) (b)

Figure 5.4: The CFHX characterization setup wrapped in with MLI.

it is important to flush the system with helium before and during cooldown. The inlet temperature of the low-pressure line is tried to keep at the same temperature at different mass flow rates. This is done to better compare measurements results.

Table 5.2: Dimensions and properties of the CFHX effectiveness characterization setup.

Variable	Value
Length CFHX	3.02 m
CFHX material	stainless steel
$D_{in,in}$	2.33 mm
$D_{in,out}$	3.00 mm
$D_{out,in}$	4.33 mm
$D_{out,out}$	5.00 mm
Length between bell jar inlet - T-sensors	0.39 m
$D_{in,in}$	1.80 mm
$D_{in,out}$	3.18 mm
Length between T-sensors - CFHX	0.13 m
$D_{in,in}$	0.66 mm
$D_{in,out}$	1.59 mm
Length between T-sensors - HX 1	0.68 m
$D_{in,in}$	3.80 mm
$D_{in,out}$	6.35 mm
Length between just before HX 1	0.06 m
$D_{in,in}$	0.66 mm
$D_{in,out}$	1.59 mm
Vacuum pressure	$< 10^{-6}$ mbar
Flow pressure	around 7.46 bar
Mass flow	between 0 and 100 mg/s
Cooldown time GM-cooler	$\approx$ 1 hour
Diameter bell jar	0.36 m
Height bell jar	0.51 m
Emissivity stainless steel	0.05

Chapter 6

Results modeling the CFHX

In this chapter the results of the CFHX modeling, which was discussed in chapter 3, are given. First, the tube-in-tube CFHX modeling results are discussed and afterwards the coiled finned tube modeling results are discussed. The chapter ends with discussing the influence of radiation.

6.1 Tube-in-tube CFHX

For the tube-in-tube CFHX modeling, the tube diameters and wall thicknesses given in table 5.2 are used. Other dimensions are possible but these dimensions are proven to be manufacturable and working. In figure 6.1 the effectiveness as function of length for the final stage CFHX, which operates between 15 K and 8 K, is plotted. Increasing the effectiveness from e.g. 96% to 97% takes a significant longer length than what is needed for increasing the effectiveness from 90% to 91%. This is because the temperature differences between the two gas streams becomes smaller at high effectiveness, which results in a lower heat transfer. From figure 6.1 it can be concluded that for the final stage CFHX a length of 17.16 m is required to fulfill the 99.8% effectiveness condition. The pressure drop for the high- and low-pressure lines are 8.5 and 11 mbars respectively, which are tolerable values. Reducing the hydraulic diameter of the circular- and annular channel by 20%, decreases the length to 14.40 m but increases the pressure drop by 100%. Also the manufacturing will be more difficult when smaller diameter tubing is used.

Similar plots can be made for CFHX 1 and CFHX 2. In the next chapter is calculated that CFHX 1 and CFHX 2 for the final stage characterization setup need a minimum effectiveness of 96%. For obtaining 96% effectiveness a length of 5.70 m is required for CFHX 1 (pressure drop 65 mbar and 122 mbar respectively) and a length of 7.20 m is required for CFHX 2 (pressure drop 12 mbar and 16 mbar respectively). In these calculations radiation is only included in the CFHX 1 calculation since this CFHX is exposed to room temperature.

An analysis has been performed on the heat transfer correlations. When the mass flow increases the Reynolds number also increases. The mass flow increases due to density increase at the cold side of the CFHX. When the mass flow hits the critical value of $Re = 2300$, the flow goes from the laminar to the turbulent regime. In the turbulent regime the heat transfer is higher which must result in a higher Nusselt number. In figure 6.2 and 6.3 the Nusselt number is plotted as function of the position in the CFHX

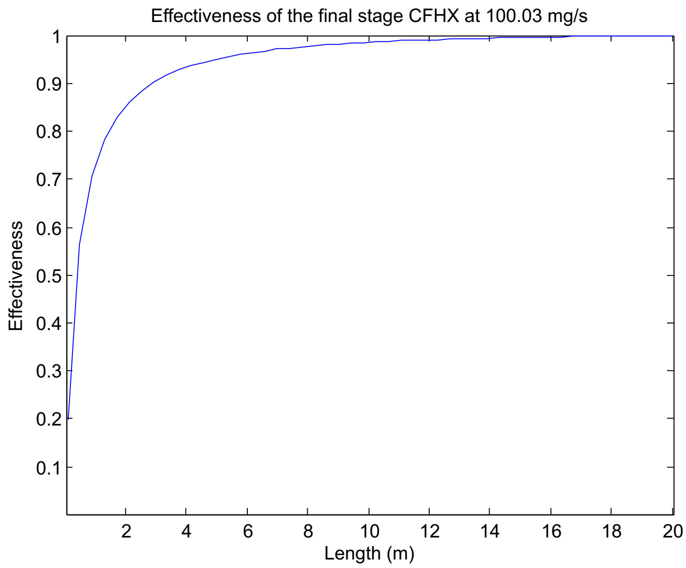

Figure 6.1: Effectiveness vs. length of a tube-in-tube CFHX.

in the high- and low-pressure channel. Due to the switch of flow regime there is a small jump between the laminar and turbulent regime. The turbulence in the high-pressure channel starts at 40 mg/s in the end part of the CFHX. This point is moving to the beginning of the CFHX for higher mass flows. The plot in figure 6.2 is taken with a mass flow of 80 mg/s. For the low-pressure channel turbulence does not occur within the mass flow range of the experiment. To model here the behavior, the mass flow is increased to 192 mg/s and $D_{out,in}$ is decreased to 3 mm, see figure 6.3. Also here a small jump is observed. For the friction factor also small jumps are observed between the laminar- and turbulent regime, see figure 6.4 and 6.5. For the low-pressure line the dimensions are again adjusted to observe turbulence. The jumps correspond well to Moody's chart [10].

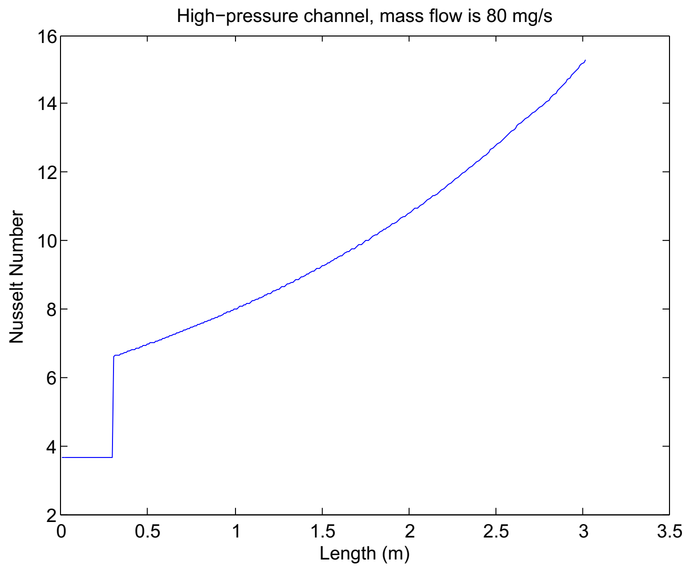

Figure 6.2: Nusselt number vs. length of a tube-in-tube CFHX. High-pressure channel, mass flow = 80 mg/s.

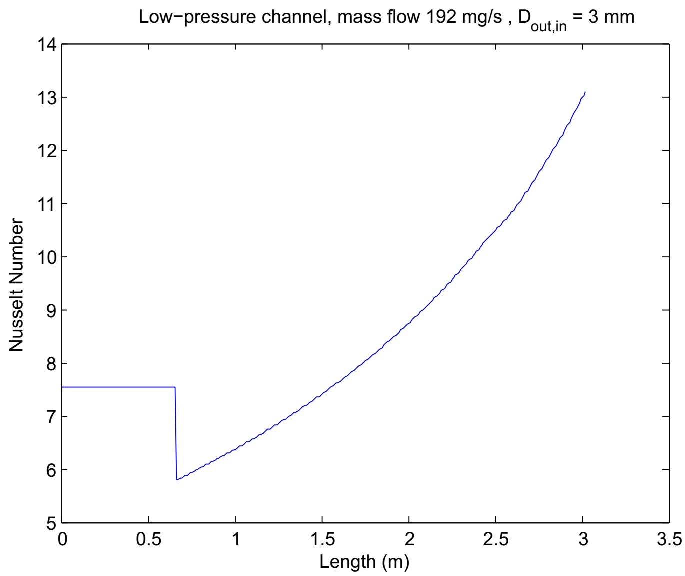

Figure 6.3: Nusselt number vs. length of a tube-in-tube CFHX. Low-pressure channel, mass flow = 192 mg/s.

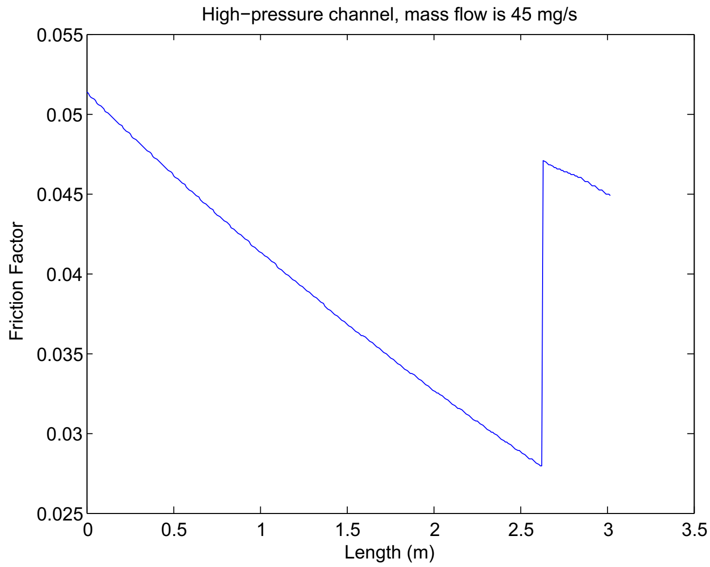

Figure 6.4: Friction factor vs. length of a tube-in-tube CFHX. High-pressure channel, mass flow = 45 mg/s.

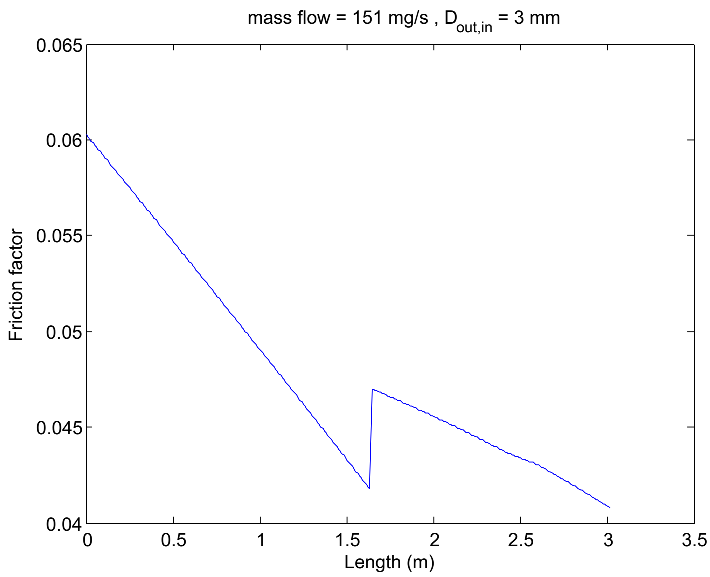

Figure 6.5: Friction factor vs. length of a tube-in-tube CFHX. Low-pressure channel, mass flow = 151 mg/s.

6.2 Coiled finned tube CFHX

In table 6.1 the dimensions used in the coiled finned tube CFHX modeling are given. These dimensions are manufacturable and have also been purchased. This corrugated tube was the smallest size available at Witzenmann. In figure 6.6 the effectiveness as function of length for the coiled finned tube CFHX is plotted. For 99.8% effectiveness a tube length of 9.85 m is needed (0.4 mbar and 0.002 mbar pressure drop respectively). For CFHX 1 (96% effective) this results in 2.50 m length (2 mbar and 0.03 mbar pressure drop, respectively) and for CFHX 2 (96% effective) this results in 3.10 m length (0.4 mbar and 0.002 mbar pressure drop, respectively).

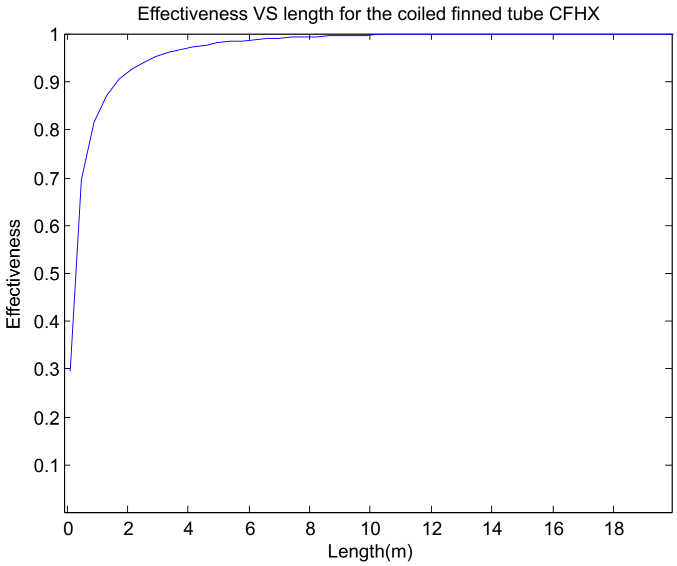

Figure 6.6: Effectiveness vs. length of a coiled tube CFHX.

Table 6.1: Dimensions of the coiled tube material.

Variable	Outer diameter (mm)	Thickness (mm)	Inner diameter (mm)	Fin pitch (mm)
Inner mandrel	25.10	0.25		
Outer tube	39.95	0.25		
Corrugated tube	7.1	0.4	4.2	1.8

6.3 Modeling the tube-in-tube CFHX without flow

Also temperatures have been measured without helium flow. To better understand these measurements a model has been made to determine the temperature in two different cases: with- and without radiation heat inleak.

6.3.1 Without radiation

When there is no flow and radiation heat inleak, the temperature profile is only determined by the conduction of heat through the helium and the tubing material. The

CFHX effectiveness characterization setup has tubing with different dimensions. These dimensions were given in table 5.2. Solving equation (3.25) results in a temperature profile given by figure 6.7. The middle part of the tubing is the CFHX. Different tubing diameters and lengths result in different slopes of the temperature profile. Equation 3.25 is solved so that there is the same heat flow in each section. This conductive heat flow turns out to be only 28 μW.

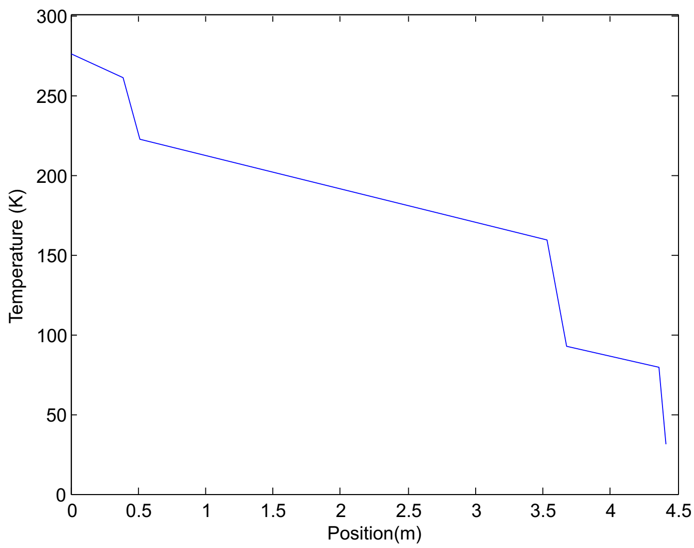

Figure 6.7: Modeled temperature profile of the tube-in-tube effectiveness characterization setup without flow and without radiation.

6.3.2 With radiation

The temperature profile without flow with radiation is given in the 'Result CFHX effectiveness characterization setup' chapter since it is plotted together with the measurement results.

6.4 Modeling the tube-in-tube CFHX with flow and radiation

In the theory chapter is was stated that the radiation distributes itself over the two pressure lines. In this section it is tried to model how this radiation distribution behaves. Three different mass flow/effectiveness profiles have been analyzed: (1) 20.8 mg/s & 98% effectiveness, (2) 99.8 mg/s & 55% effectiveness and (3) 99.8 mg/s & 91% effectiveness. These temperature profiles are given in figure 6.8, 6.9 and 6.10 respectively. In figure 6.8 the blue colored line is the temperature profile of the high- and low-pressure line without radiation. Here the top line is the temperature profile of the high-pressure line and the bottom line is the temperature profile of the low-pressure line. When the radiation is turned on and increased, the temperature profile rises (green, orange and red line). The higher the radiation the higher the increase in temperature. The inlet temperatures of the high- and low-pressure lines are fixed. The effect of radiation is an increases in the outlet temperatures of the high- and low-pressure line. The increase in outlet temperature is mainly in the high-pressure line since the temperature of the low-pressure line outlet cannot rise that much due to the high effectiveness ($T_{pL,out}$ is already close to $T_{pH,in}$). The table under the figures indicate what percentage of radiation is going to the low-pressure line and what percentage of radiation is going to the high-pressure line.

Similar plots have been made for higher mass flow in figure 6.9 and figure 6.10. In figure 6.9 the effectiveness is lower. This results in most of the radiation distributing to the low-pressure line. In figure 6.10 the effectiveness is higher which results in most of the radiation distributing to the high-pressure line.

In general it is hard to predict how the radiation exactly distributes over a CFHX. At low effectiveness the radiation will mostly distribute to the low-pressure channel and at an effectiveness of around 90% or higher the radiation will mostly distribute to the high-pressure channel. More modeling results, e.g. radiation influence and effectiveness vs. mass flow, are given in the next two chapters. Here the modeling results are combined with the experimental results.

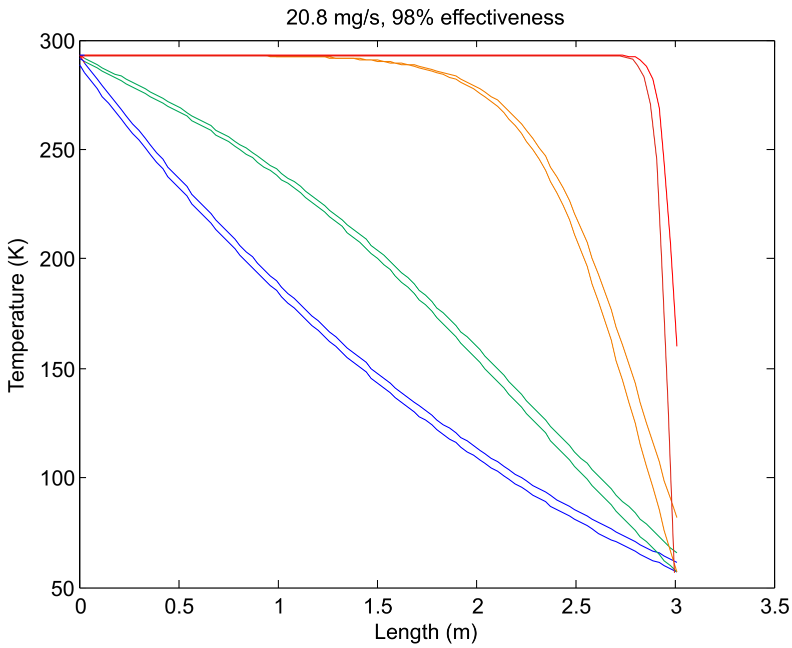

$\dot{Q}_{rad}(W)$	$\dot{Q}_{rad}\,p_L(\%)$	$\dot{Q}_{rad}\,p_H(\%)$
0.74	40.54	59.46
2.70	17.78	82.22
11.1	4.32	95.68

Figure 6.8: Radiation distribution of a 98% effective CFHX with a mass flow of 20.8 mg/s.

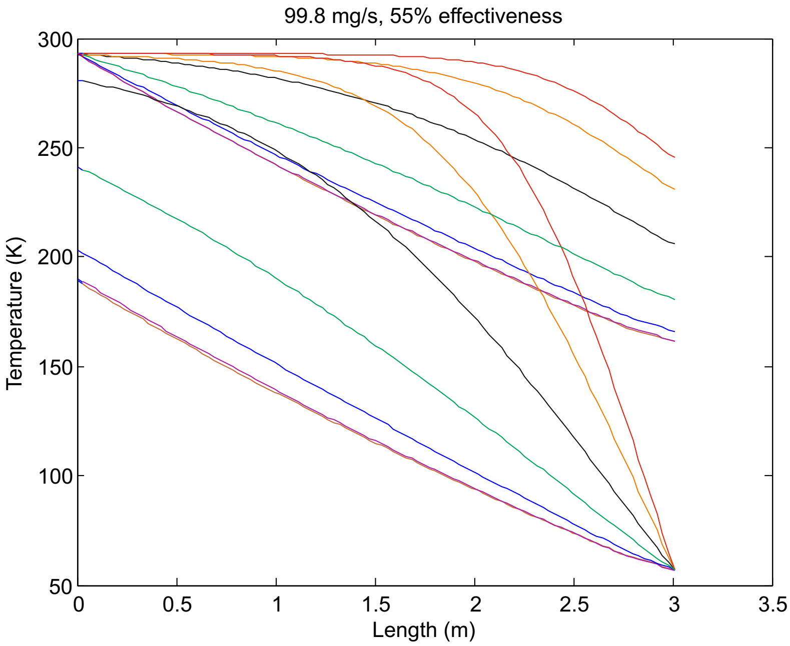

$\dot{Q}_{rad}$	$\dot{Q}_{rad}p_L(\%)$	$\dot{Q}_{rad}p_H(\%)$
1.03	83.50	16.50
10.2	75.78	24.22
37.44	73.08	26.92
70.93	67.46	32.54
89.72	59.92	40.08
97.73	55.39	44.61

Figure 6.9: Radiation distribution of a 55% effective CFHX with a mass flow of 99.8 mg/s.

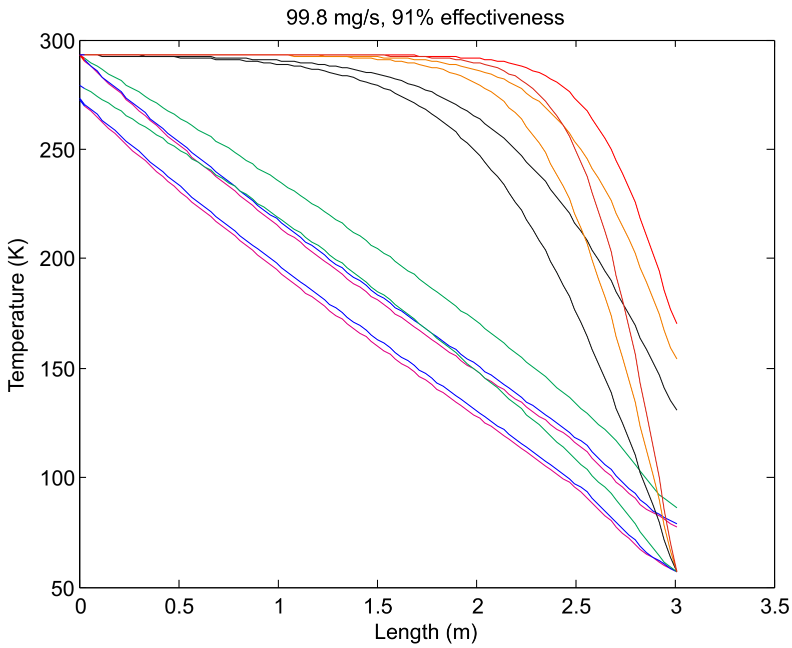

$\dot{Q}_{rad}(W)$	$\dot{Q}_{rad}p_L(\%)$	$\dot{Q}_{rad}p_H(\%)$
0.89	51.69	48.31
8.2	46.48	53.52
39.62	27.78	72.22
50.35	21.31	78.69
58.98	18.22	81.78

Figure 6.10: Radiation distribution of a 91% effective CFHX with a mass flow of 99.8 mg/s.

Chapter 7

Results final stage characterization setup

In this chapter the results of the final stage characterization setup modeling are presented. The theory of the modeling was already presented in chapter 5 and a schematic picture of the setup was given in figure 4.1. For the analysis of the final stage characterization setup the dimensions and properties given in table 7.1 are used. The dimensions of the radiation shields are chosen so that the CFHXs will fit between the radiation shields.

7.1 System analysis

In this section, pre-cooling to 15 K is analyzed. To reach a second stage temperature of 15 K a minimum effectiveness of CFHX 1 and CFHX 2 and a minimum cooling power of both stages of the GM-cooler is required. When CFHX 1 is very effective, CFHX 2 can be made less effective and vice versa. Also when the GM-cooler is more powerful the CFHXs length can be reduced. The cooling power of the GM-cooler can be found in the load curve plot of figure 4.2. Equation (4.4) can be solved for T_1 and T_2 for different combinations of effectiveness for CFHX 1 and CFHX 2. Figure 7.1 gives effectiveness combinations which result in a second stage temperature < 15 K. The combination of both CFHXs at 96% effectiveness is the preferable combination since this minimizes the combined CFHXs length, see also figure 7.2. In the modeling result chapter the lengths of these CFHXs were calculated. When using an effectiveness of 96% the first- and second stage of the GM-cooler reach the temperatures given in table 7.2. The 14.49 K temperature of the first stage can be controlled to 15 K with a heater. The heat inleaks depicted in figure 4.1 are summarized in table 7.3 for the case that both CFHXs are 96% effective. The largest heat inleaks are $\dot{Q}_{MLI}$ and $\dot{Q}_{con1}$. The other heat inleaks are low and can be neglected. Lowering of $\dot{Q}_{MLI}$ can be established by adding more layers of MLI onto the first stage radiation shield and lowering of $\dot{Q}_{con1}$ can be done by increasing the length of the wiring. In the analysis it is assumed that the heat exchange in HX 1 and HX 2 is perfect, so that the outlet temperature of the helium gas equals the GM-cooler stage temperature. This assumption is validated in the next section.

Table 7.1: Dimensions and properties of the final stage characterization setup.

Variable	Value
Diameter bell jar	0.36 m
Diameter 1st stage radiation shield	0.26 m
Diameter 2nd stage radiation shield	0.16 m
Diameter final stage HX	0.06 m
Height bell jar	0.51 m
Height 1st stage radiation shield	0.41 m
Height 2nd stage radiation shield	0.31 m
Height final stage HX	0.01 m
Length wires between stages	0.33 m
Diameter manganin wire	0.1 mm
Diameter copper wire	0.4 mm
ε copper	0.05
Number of layers MLI (N_S)	10

Table 7.2: Temperatures of the first- and second stage when CFHX 1 and CFHX 2 are 96% effective.

Variable	Value
T_{HX1in}	55.56 K
T_1	45.67 K
T_{HX2in}	15.49 K
T_2	14.49 K

Table 7.3: Heat loads when CFHX 1 and CFHX 2 are 96% effective.

Variable	Value
$\dot{Q}_{MLI}$	1.12 W
$\dot{Q}_{rad12}$	0.002 W
$\dot{Q}_{rad23}$	0.004 mW
$\dot{Q}_{con1}$	0.23 W
$\dot{Q}_{con12}$	0.067 W
$\dot{Q}_{con23}$	0.004 W

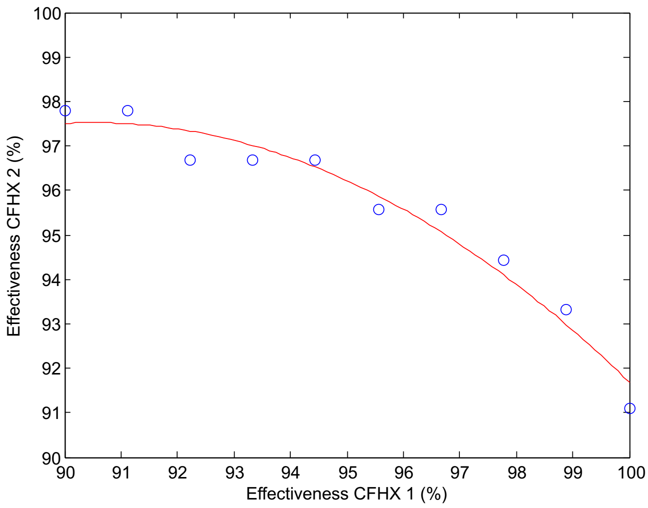

Figure 7.1: Effectiveness CFHX 1 vs. effectiveness CFHX 2 to obtain $T_2 < 15$ K. The blue circles are the different modeled combinations and the red line is a fit through these circles.

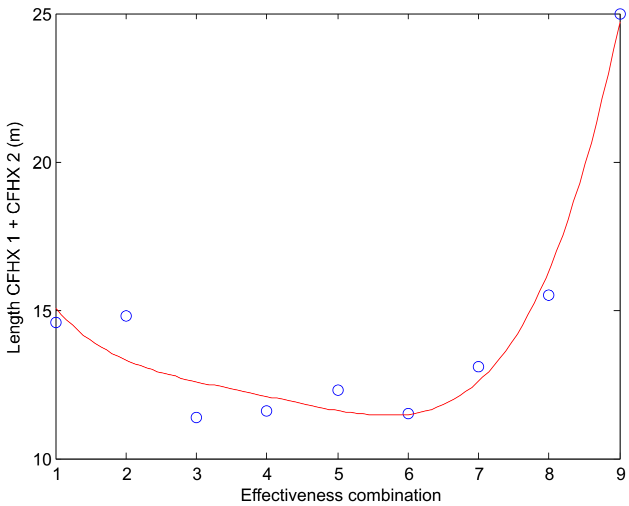

Figure 7.2: Length CFHX 1 + CFHX 2 vs. combination effectiveness from figure 7.1. The most left dot in figure 7.1 corresponds to combination 1 in this figure and so on. The CFHX 1 = 100% combination is left out of this figure since this is physically not possible. The blue circles are the different modeled combinations and the red line is a fit through these circles.

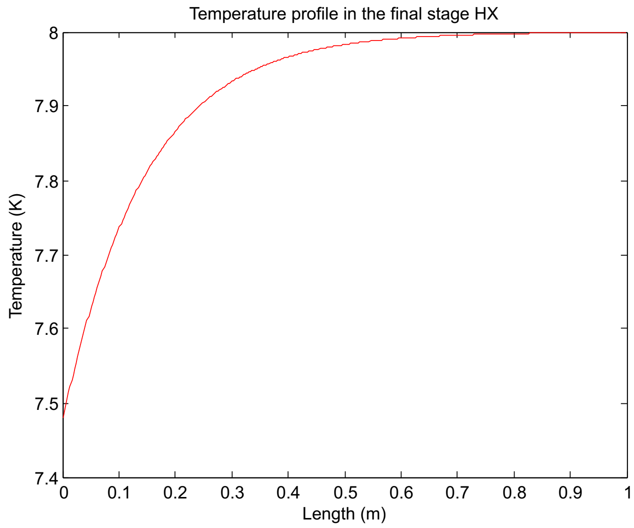

Figure 7.3: Temperature profile in the final stage HX.

7.2 Final stage HX

The final stage HX will be a copper block with square grooves machined into it. The cross-sectional area of these groves will be 2.3 mm^2. A picture of such a copper block was given in figure 5.2, indicated as HX 1. Figure 3.8 showed a schematic configuration of this CFHX. Solving equation (3.3), results in the temperature profile of the final stage HX given by figure 7.3. It can be seen that the temperature reaches 8 K within a length of 1 m and the pressure drop is only 0.55 mbar. A similar analysis has been carried out for HX 1 ($L = 0.7$ m) and HX 2 ($L = 1.0$ m) [30]. Using these lengths the temperatures go from T_{HX1in} to T_1 and from T_{HX2in} to T_2 within these lengths. The pressure drop is also low, namely 2.4 mbar for HX 1 and 0.58 mbar for HX 2.

7.3 Mass flow through the restriction

The use of restrictions with circular cross section will reduce the chance of clogging. In circular cross sections the length- and width are maximized so ice crystals have the highest ease to flow through.

In the theory chapter it was stated that the helium density increases at low temperature. At 8 K the density of the helium increases by a factor of 30 compared to room temperature and the dynamic viscosity decreases by a factor 7 compared to room temperature. This results in a 210 times larger mass flow at 8 K. An initial room temperature mass flow of 0.5 mg/s will then become 100 mg/s @ 8 K.

Using equation (4.7) the length of the restriction can be plotted vs. the diameter of the restriction. This plot is given in figure 7.4. When D increases, L needs to be increased to the 4th power to keep the same mass flow rate. Having a larger diameter is in favor for preventing clogging, since ice crystals can flow easier through a larger restriction. Therefore a long length restriction such as a capillary tube is recommended.

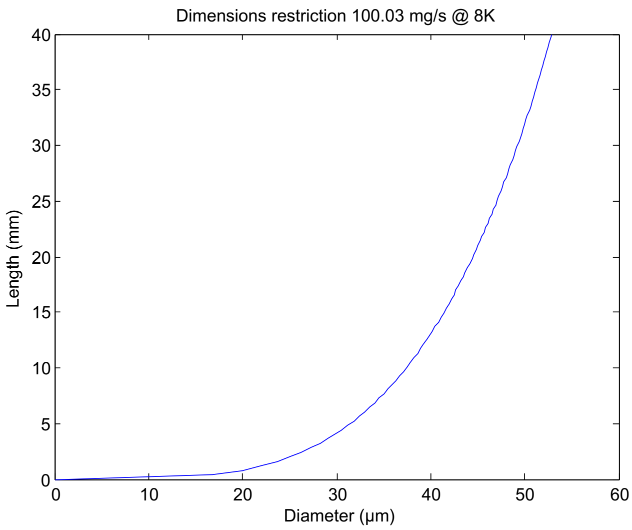

Figure 7.4: Length plotted vs. the diameter of the restriction to obtain 100.03 mg/s @ 8 K.

Chapter 8

Results CFHX effectiveness characterization setup

In this chapter the results of the effectiveness characterization setup, which was introduced in chapter 5, are discussed.

The temperature of the four in- and outlets of the CFHX, the temperature of HX 1 and the pressure are measured. This is done at four different mass flow rates. At each mass flow it was important to wait until equilibrium of the temperatures sets in. The results of the CFHX effectiveness characterization setup measurement are given in table 8.1. From these measurement several quantities can be calculated which are given in table 8.2. Note that the Δ in the enthalpy represents a difference and that the Δ in the effectiveness and radiation represents an error.

Table 8.1: Measurement results CFHX effectiveness characterization setup.

	$massflow(mg/s)$				
	0	9.77	19.80	49.67	99.62
$T_{pH,in}(K)$	276.06	290.75	291.77	292.49	292.92
$T_{pH,out}(K)$	273.86	88.25	84.91	85.46	88.78
$T_{pL,in}(K)$	274.57	72.81	72.79	72.64	72.87
$T_{pL,out}(K)$	275.41	286.34	286.59	283.78	279.27
$T_{HX1}(K)$	30.78	64.61	67.81	69.87	71.31
$p(bar)$	4.35	7.74	7.90	8.46	9.78

It can be concluded that there is radiation heat inleak into the setup since $\Delta\dot{H}_{pH} < \Delta\dot{H}_{pL}$. The difference in enthalpy change cannot be due to a sudden pressure drop in the system. If for example the pressure in the 9.77 mg/s measurement drops by half in HX 1 this only results in an enthalpy difference of 9.4 mW between the gas streams. The effectiveness as function of mass flow is plotted in figure 8.1.
In this figure the squares are the ϵ_{min} and the circles are the ϵ_{max} with their error bars. From this figure it can be concluded that there is an error due to the difference between ϵ_{min} and ϵ_{max} and an error due to the error in ϵ_{min} and ϵ_{max}. Adding these errors results in for example an effectiveness of 93.05±1.10% at 99.62 mg/s. This corresponds with the modeled effectiveness of 93.10%. At lower mass flow the effectiveness increases. This is due to a lower enthalpy flow of the helium gas stream, which therefore more

Table 8.2: Quantities calculated from CFHX effectiveness characterization setup results.

	$massflow(mg/s)$			
	9.77	19.80	49.67	99.62
$\Delta\dot{H}_{pH}(W)$	10.28	21.28	53.43	105.61
$\Delta\dot{H}_{pL}(W)$	10.84	22.00	54.50	106.87
$\Delta\dot{H}_{max}(W)$	11.06	22.53	56.75	113.93
$\dot{Q}_{rad}(W)$	0.56	0.72	1.07	1.26
$\Delta\dot{Q}_{rad}(W)$	0.09	0.17	0.43	0.87
$\epsilon_{max}(\%)$	97.98	97.64	96.04	93.80
$\Delta\epsilon_{max}(\%)$	0.36	0.36	0.35	0.35
$\epsilon_{min}(\%)$	92.90	94.45	94.15	92.70
$\Delta\epsilon_{min}(\%)$	0.76	0.76	0.76	0.76

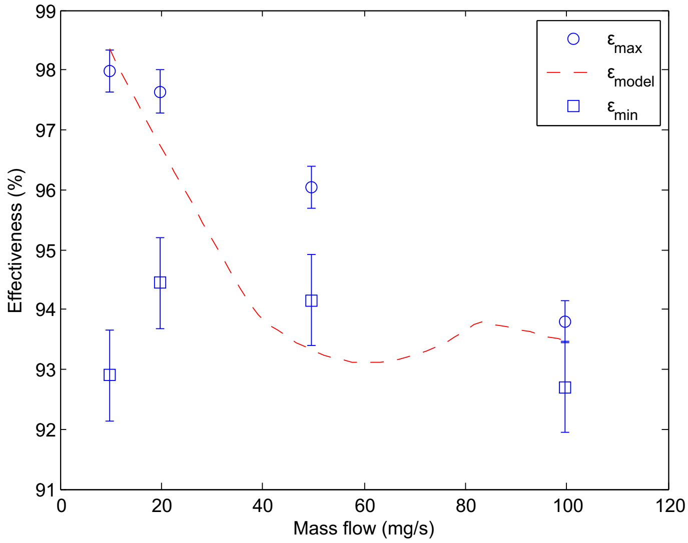

Figure 8.1: Effectiveness vs. mass flow. The squares are the ϵ_{min} and the circles are the ϵ_{max} with their error bars. The dashed line is the modeling result.

easily can adopt to the temperature of the counter flowing gas stream. The effect of radiation becomes larger at low mass flow rate, which can be seen in a larger spread between ϵ_{min} and ϵ_{max}. At low mass flow, the enthalpy flow is low and therefore more easily influenced by radiation. In all measurements ϵ_{max} will be the most likable value since the effectiveness is high. The modeled effectiveness (dashed lines) corresponds to the measurements within the error bars. The rise in effectiveness in the region between 60 mg/s and 85 mg/s is due to the occurrence of turbulence, which starts at 40 mg/s. In this region the increase in effectiveness by turbulence is higher than the decrease in effectiveness caused by the higher enthalpy flow. At mass flows higher than 85 mg/s the turbulence is still present but the increase in enthalpy flow dominates.

The radiation as function of mass flow has been plotted in figure 8.2. At low mass flow this radiation can be measured most accurately. The radiation increases at higher mass flow due to the fact that the temperature profile lowers and becomes less curved, so a larger temperature difference occurs between the CFHX and ambient, resulting in a higher radiation.

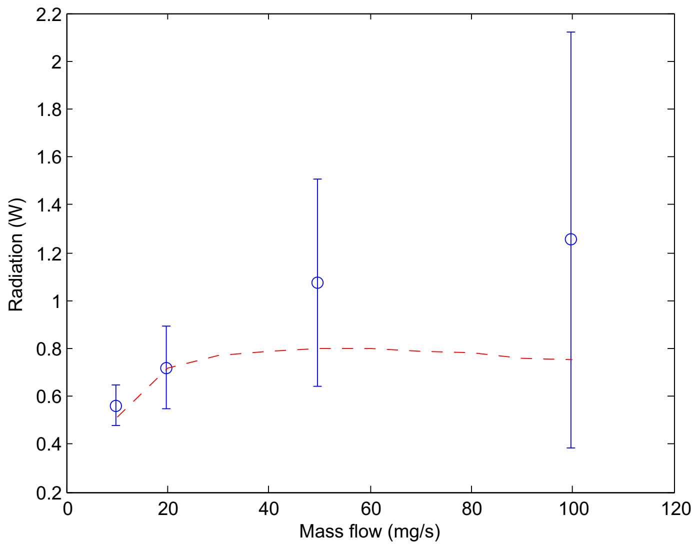

Figure 8.2: $\dot{Q}_{rad}$ vs. mass flow, fitted with model (dashed line).

The assumption in the model that $T_{pL,in}$ equals T_1 turns out to be quite valid since at 99.62 mg/s the temperature difference between T_{HX1} and $T_{pL,in}$ only differs by 1.56 K. The real temperature difference might even be lower since there is tubing under influence of radiation between T_{HX1} and $T_{pL,in}$. The temperature of the first stage during the 99.62 mg/s measurement is 71.31 K. When using equation (4.4) and using the minimum measured effectiveness of 91.94% a first stage temperature of 60.06 K is obtained. The higher measured temperature might be explained by the use of less MLI around the first stage of the GM-cooler during the CFHX effectiveness measurement as compared to the load curve measurement.

The temperatures are measured at different positions in the CFHX characterization setup, see also figure 5.1. The temperature profile of the 99.62 mg/s measurement is given in figure 8.3. Here the circles are measured temperature points and the dashed line is the CFHX modeling result. The middle part represents the CFHX and the most left circle is the entrance temperature and the most right circle is the temperature of the GM-cooler. A similar plot is given for the 9.77 mg/s measurement in figure 8.4.

Due to radiation and an increased effectiveness the temperatures at the 'hot' side get closer to each other at low mass flow. At the 'cold' side the temperatures get initially closer to each other due to the increase of effectiveness at low mass flow. This effect is opposed by the radiation heat inleak which dominates the temperature profile when the mass flow gets even lower. This results can be seen by the $T_{pH,out}$-values in table 8.1.

When there is no flow, a temperature profile given by figure 8.5 is obtained. The model that includes radiation indicates that just shortly before the GM-cooler the tem-

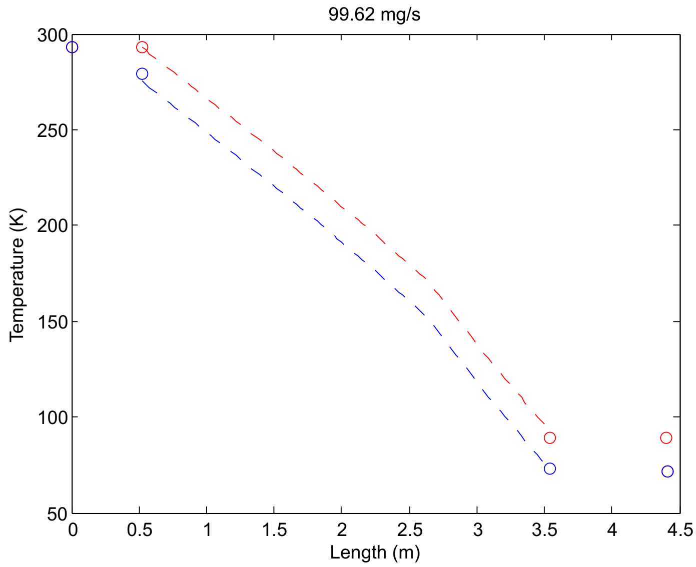

Figure 8.3: CFHX temperature profile. Mass flow is 99.62 mg/s. Dots are the measurement points and dashed lines are modeling results.

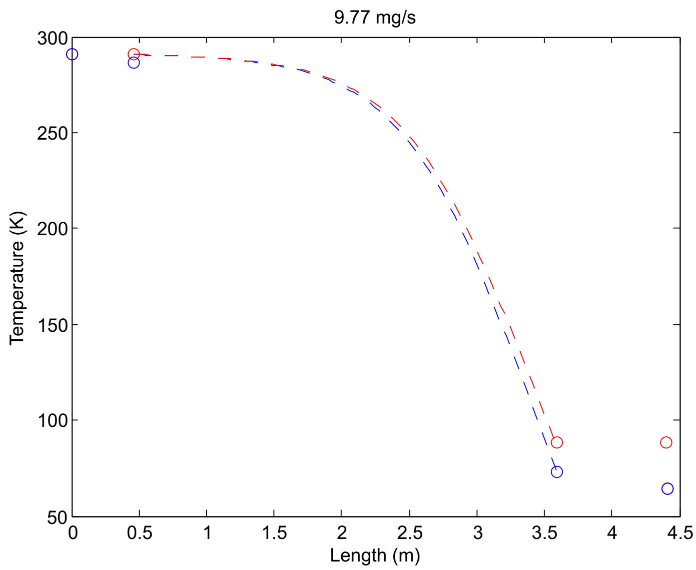

Figure 8.4: CFHX temperature profile. Mass flow is 9.77 mg/s. Dots are the measurement points and dashed lines are modeling results.

perature of the tubing decreases. Including radiation thus completely changes the temperature profile initially given by figure 6.7. This modeling result agrees with the measurement so radiation had a large influence onto the setup. This can be explained by the fact that the radiation is in the watt range and the conduction in the microwatt range. In the calculations a stainless steel emissivity of 0.1 was assumed. A zoomed in version of figure 8.5 is given by figure 8.6. It can be seen that just 0.01 m before HX 1 the temperature drops. Normally the effectiveness can also be obtained by measuring the cooling power needed to keep the cold end of the CFHX at the same temperature, see also equation (2.10), but due to radiation heat inleak this measured effectiveness turned out to be unreliable.

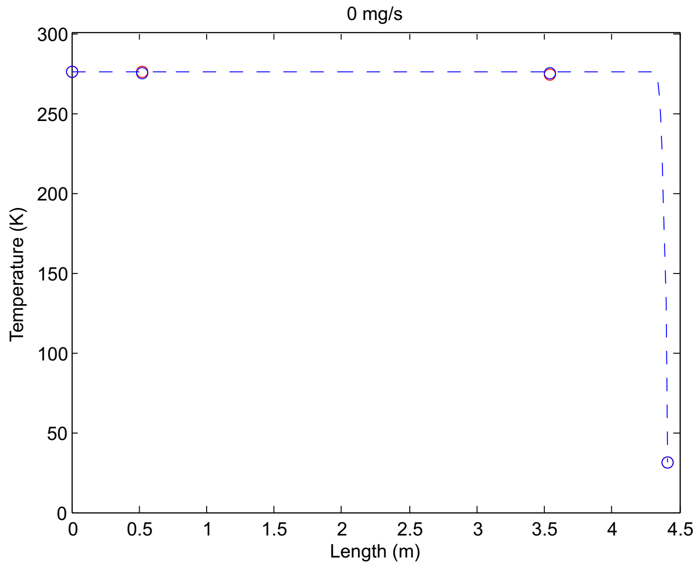

Figure 8.5: Modeled CFHX temperature profile with radiation. Mass flow is 0 mg/s. Dots are the measurement points and dashed lines are modeling results.

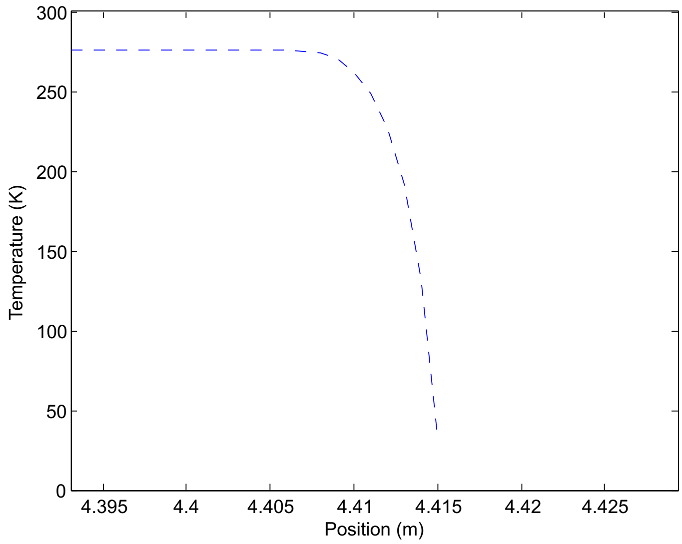

Figure 8.6: Modeled CFHX temperature profile with radiation, zoomed in. Mass flow is 0 mg/s. Dots are the measurement points and dashed lines are modeling results.

Chapter 9

Discussion

The final stage characterization setup still needs to be build. Building such a setup takes a lot of time and was not possible within the time span of this research. The effectiveness of a tube-in-tube CFHX was determined in a CFHX effectiveness measurement setup. This setup was influenced by radiation heat inleak. To minimize the radiation heat inleak in future experimental setups, the setup needs to be surrounded with a low temperature radiation shield. In the final stage characterization setup a final stage entrance temperature of 15 K is required. To reach this a trade-off has to be made between long pre-cooling CFHXs (CFHX 1 & CFHX 2) or a powerful pre-cooling GM-cooler. The latter can decrease the system size significantly. The final stage CFHX still needs a long length (17.16 m) so the dimensions of a bell jar have to be taken into account. A larger bell jar than the one used in the CFHX characterization setup might be needed, since in this setup the 3.02 m tube-in-tube CFHX just fitted. Materials to build a coiled tube CFHX had been ordered. Fabrication and testing the characteristics of this type of CFHX in a CFHX characterization setup with radiation shields still needs to be done.

Chapter 10

Conclusions

An analysis of the final stage has been performed. The final stage heat exchanger can be relatively short with a length of 1 m and the Joule-Thomson throttle needs to be a small restriction in the μm range. In the final stage characterization setup CFHX 1 and CFHX 2 need a minimum effectiveness of 96% for the temperature of the second stage to reach 15 K. The final stage CFHX (CFHX 3) needs to have an effectiveness of 99.8%. Two CFHXs have been analyzed in detail for the final stage CFHX: the tube-in-tube CFHX and the coiled finned tube CFHX. The tube-in-tube CFHX needs to have length of 17.16 m and the coiled finned tube CFHX needs to have a length of 9.85 m to reach 99.8% effectiveness. To test the performance of CFHXs a CFHX effectiveness characterization setup has been build. In this setup a 3.02 m long tube-in-tube CFHX has been tested. Due to radiation heat inleak a radiation error entered into the effectiveness. At 99.62 mg/s the modeled effectiveness of 93.10% agrees within the measured effectiveness of 93.05±1.10%. A 17.15 m long tube-in-tube CFHX therefore might be a good candidate for the final stage CFHX. A future effectiveness characterization setup needs to have a radiation shield to minimize the radiation heat inleak, which increases the accuracy of the measurement.

Nomenclature

A	Area	[m^2]
C	Heat Capacity	[$J \cdot K^{-1}$]
C_r	Empirical constant	[-]
C_R	Capacity ratio	[-]
C_s	Empirical constant	[-]
D	Diameter	[m]
D_H	Hydraulic diameter	[m]
F	View factor	[-]
$\dot{H}$	Enthalpy flow rate	[J]
L	Length	[m]
N	Layer density	[m^{-1}]
N_p	Number of passes	[-]
N_s	Total numbers of layers	[-]
N_{tu}	Number of transfer units	[-]
P	Cooling power	[W]
P	Perimeter	[m]
$\dot{Q}$	Heat transfer rate	[W]
S_L	Longitudinal pitch	[-]
S_T	Transverse pitch	[-]
T	Temperature	[K]
U	Overall heat transfer coefficient	[$W \cdot m^{-2} \cdot K^{-1}$]
W	Mass flow	[$kg \cdot h^{-1}$]
c_p	Specific heat capacity	[$J \cdot kg^{-1} \cdot K^{-1}$]
f	Friction factor	[-]
h	Specific enthalpy	[$J \cdot kg^{-1}$]
h	Heat transfer coefficient	[$W \cdot m^{-2} \cdot K^{-1}$]
$\dot{m}$	Mass flow rate	[$kg \cdot s^{-1}$]
p	Pressure	[Pa]
s	Specific entropy	[$J \cdot kg^{-1} \cdot K^{-1}$]

CFHX	Counterflow heat exchanger	[-]
GM	Gifford-McMahon	[-]
HX	Heat exchanger	[-]
JT	Joule-Thomson	[-]
MLI	Multi-layer insulation	[-]
Nu	Nusselt number	[-]
Pr	Prandtl number	[-]
Re	Reynolds number	[-]
ϵ	Effectiveness	[-]
η_0	Fin efficiency	[-]
η_f	Adiabatic fin efficiency	[-]
ε	Emissivity	[-]
λ	Thermal conductivity	[$\mathrm{W \cdot m^{-1} \cdot K^{-1}}$]
μ	Dynamic fluid viscosity	[$\mathrm{Pa \cdot s}$]
μ_{JT}	Joule-Thomson coefficient	[$\mathrm{K \cdot Pa^{-1}}$]
ν	Kinematic fluid viscosity	[$\mathrm{m^2 \cdot s^{-1}}$]
ρ	Density	[$\mathrm{kg \cdot m^{-3}}$]
σ	Stefan-Boltzmann constant	[$\mathrm{W \cdot m^{-2} \cdot K^{-4}}$]

References

[1] Wikipedia, "European Extremely Large Telescope," http://en.wikipedia.org/wiki/European_Extremely_Large_Telescope.

[2] ESO, "The European Extremely Large Telescope," www.eso.org/sci/facilities/eelt/docs/E-ELT_2013-04-02.pdf.

[3] . M. consortium, "The Mid-infrared E-ELT Imager and Spectrograph," http://metis.strw.leidenuniv.nl/index.php.

[4] ESO, "An artist's impression of the E-ELT," http://www.eso.org/public/images/elt-2011-02-cc/.

[5] H.J.M. ter Brake, Y. Wu, D.R. Zalewski, C.H. Vermeer, H.J. Holland, J. Doornink, B. Benthem, and E. Boom, *Sorption-based vibration-free cooler for the METIS instrument on E-ELT*, poster.

[6] D. Zalewski, "Sorption-based cooler chain design for the E-ELT METIS instrument," Tech. rep. (11 June 2012).

[7] R. Roelfsema, "METIS Thermal design and analysis," Tech. rep. (21-09-2009), issue: 2.

[8] Y. Wu, "Presentation E-ELT meeting 20121015," .

[9] LakeShore, *Temperature Measurement and Control book*.

[10] A. Bejan, *Heat transfer* (John Wiley & Sons, Inc., 1993). http://books.google.nl/books?id=TgtRAAAAMAAJ

[11] C. Keller, G. Cunnington, and A. Glassford, "Thermal performance of multilayer insulations, NASA Technical Report," (1974).

[12] "Cryogenic infrared mission JAXA/SPICA with advanced cryocoolers," Cryogenics **46**, 149 – 157 (2006).

[13] JANIS, "Daikin GM-JT Cryocoolers from Janis and Sumitomo (SHI)," http://www.janis.com/products/productsoverview/DaikinGifford-McMahonJoule-ThomsonCryocoolers.aspx#.

[14] "Private communication with Sumitomo (SHI) Cryogenics of Europe GmbH," .

[15] R. C. Clauss, *Cryogenic Refrigeration Systems*.

[16] e. a. Hong, Y-J, "A numerical study of the performance of a heat exchanger for miniature Joule-Thomson refrigerator," in *Cryocoolers 15, edited by S.D. Miller and R.G. Ross, Jr.* **International Cryocooler Conference Press, Boulder, CO**, pp. 379–386 (2009).

[17] D. Bullock, "Goldstone NASA Deep Space Network," http://eecue.com/p/31797/MASER-Unit.html.

[18] L. S. C. Inc, *Appendix D: Sensor Calibration Accuracies*, http://www.lakeshore.com/Documents/LSTC_appendixD_l.pdf.

[19] S. WEKA AG, CH-8344 Bretswil, "Dimensions for Standard Cryogenic Valve PN25, Bellows Sealed, with Pneumatic Actuator, WEKA Specification no. 19930219," .

[20] J. Zimmerman, T. Flynn, U. S. N. B. of Standards, and U. S. O. of Naval Research, *Applications of closed-cycle cryocoolers to small superconducting devices: proceedings of a conference held at the National Bureau of Standards, Boulder, Colorado, October 3-4, 1977*, NBS special publication (U.S. Dept. of Commerce, National Bureau of Standards : for sale by the Supt. of Docs., U.S. Govt. Print. Off., 1978).
http://books.google.nl/books?id=xYVR0pCDu-QC

[21] "Weka cryo datasheet," http://seongwooinst.com/weka/cryo_datasheets.pdf.

[22] R. Shah and D. Sekulic, *Fundamentals of Heat Exchanger Design* (Wiley, 2003).
http://books.google.nl/books?id=beSXNAZblWQC

[23] G. Hewitt, *Heat Exchanger Design Handbook, 1998*, Heat Exchanger Design Handbook, 1998 (Begell House, 1998).
http://books.google.nl/books?id=qVFGAAAAYAAJ

[24] R. Barron, *Cryogenic Heat Transfer*, Series in Chemical and Mechanical Engineering (Taylor and Francis, 1999).
http://books.google.nl/books?id=8fZ6-Nl491EC

[25] K. A. Gardner, "Efficiency of extended surfaces, Trans. ASME, Vol.67, pp. 621-631, 1945," .

[26] T. Bergman, F. Incropera, A. Lavine, and D. DeWitt, *Fundamentals of Heat and Mass Transfer* (Wiley, 2011).
http://books.google.nl/books?id=vvyIoXEywMoC

[27] Witzenmann, "Corrugated tube," http://www.witzenmann.be/witzenmann/vdbbe/produkte/wellschlaeuche.php.

[28] Mankernberg, "Calculation of Pressure Regulators," http://www.mankenberg.de/en/171/en/77/UPLOAD/pdf/s33_1.pdf.

[29] "Bronkhorst Calibration Certificate, Certificate No. BHT177/1387246," .

[30] P. van den Bosch, *Cryocooler-operated High-Tc SQUID System for Magnetocardiography in an Unshielded Environment*, Ph.D. thesis (1996).
http://books.google.nl/books?id=U8U2AAAACAAJ

Appendix

10.1 Other measurements

More measurements have been performed. In these measurements no or less MLI was used around the CFHX compared to the measurement given in the result section. The results of these measurements are given in table 10.1 and 10.2. In these measurements the radiation heat inleak is larger. Therefore these measurements are left outside the scope of the thesis.

Table 10.1: Measurement results CFHX effectiveness characterization setup with MLI placed only on the tubing going from and to the CFHX.

	$massflow(mg/s)$				
	0	9.60	20.27	49.46	99.80
$T_{pH,in}(K)$	273.93	291.39	292.33	292.57	293.02
$T_{pH,out}(K)$	269.30	55.53	51.96	57.01	74.60
$T_{pL,in}(K)$	271.73	37.65	36.93	41.99	57.17
$T_{pL,out}(K)$	273.42	287.27	286.40	281.94	277.93
$T_{HX1}(K)$	28.56	30.45	33.06	40.42	56.74
$p(bar)$	5.10	7.77	7.84	8.06	8.86

Table 10.2: Measurement results CFHX effectiveness characterization setup without MLI.

	$massflow(mg/s)$		
	0	10.13	100.13
$T_{pH,in}(K)$	287.74	291.79	293.41
$T_{pH,out}(K)$	286.90	94.77	96.36
$T_{pL,in}(K)$	288.44	63.40	78.87
$T_{pL,out}(K)$	286.70	288.60	280.82
$T_{HX1}(K)$	32.95	42.1	77.36
$p(bar)$	3.66	7.8	8.89

10.2 Error calculation

The error in ϵ from equation (2.9) is given by:

$$\begin{aligned}
\epsilon &= \frac{\Delta h_{pL}}{min\left[\Delta h_{max(pH)}, \Delta h_{max(pL)}\right]} \\
\left(\frac{\Delta\epsilon}{\epsilon}\right)^2 &= \left(\frac{\Delta(\Delta h_{pL})}{\Delta h_{pL}}\right)^2 + \left(\frac{\Delta min[\Delta h_{max(pH)}, \Delta h_{max(pL)}]}{min\left[\Delta h_{max(pH)}, \Delta h_{max(pL)}\right]}\right)^2 \\
\left(\frac{\Delta\epsilon}{\epsilon}\right)^2 &= \left(\frac{\Delta\left(h_{T_{pL,out}} - h_{T_{pL,in}}\right)}{\Delta h_{pL}}\right)^2 + \left(\frac{\Delta\left[c_{p_{min(T_{pH,in})}}\Delta T - c_{p_{min(T_{pH,in})}}\Delta T\right]}{min\left[\Delta h_{max(pH)}, \Delta h_{max(pL)}\right]}\right)^2 \\
\left(\frac{\Delta\epsilon}{\epsilon}\right)^2 &= \left(\frac{\sqrt{\left[\Delta h_{T_{pL,out}}\right]^2 + \left[\Delta h_{T_{pL,in}}\right]^2}}{\Delta h_{pL}}\right)^2 + \left(\frac{\sqrt{\left[c_{p_{min(T_{pH,in})}}\Delta T\right]^2 + \left[c_{p_{min(T_{pL,in})}}\Delta T\right]^2}}{min\left[\Delta h_{max(pH)}, \Delta h_{max(pL)}\right]}\right)^2 \\
\left(\frac{\Delta\epsilon}{\epsilon}\right)^2 &= \left(\frac{\sqrt{\left[c_{p(pL,T_{out})}\Delta T\right]^2 + \left[c_{p(pL,T_{in})}\Delta T\right]^2}}{\Delta h_{pL}}\right)^2 + \left(\frac{\sqrt{\left[c_{p_{min(T_{pH,in})}}\Delta T\right]^2 + \left[c_{p_{min(T_{pL,in})}}\Delta T\right]^2}}{min\left[\Delta h_{max(pH)}, \Delta h_{max(pL)}\right]}\right)^2 \\
\Delta\epsilon &= \epsilon\sqrt{\left(\frac{\sqrt{\left[c_{p(pL,out)}\Delta T\right]^2 + \left[c_{p(pL,in)}\Delta T\right]^2}}{\Delta h_{pL}}\right)^2 + \left(\frac{\sqrt{\left[c_{p_{min(T_{pH,in})}}\Delta T\right]^2 + \left[c_{p_{min(T_{pL,in})}}\Delta T\right]^2}}{min\left[\Delta h_{max(pH)}, \Delta h_{max(pL)}\right]}\right)^2}
\end{aligned} \tag{10.1}$$

The error in $\dot{Q}_{rad}$ from equation (2.11) is given by:

$$
\begin{aligned}
\dot{Q}_{rad} &= \Delta\dot{H}_{pL} - \Delta\dot{H}_{pH} \\
\dot{Q}_{rad} &= \dot{m}\left(h_{T_{pL,out}} - h_{T_{pL,in}}\right) - \dot{m}\left(h_{T_{pH,in}} - h_{T_{pH,out}}\right) \\
\dot{Q}_{rad} &= \dot{m}\left(h_{T_{pL,out}} - h_{T_{pL,in}} - h_{T_{pH,in}} + h_{T_{pH,out}}\right) \\
\left(\frac{\Delta\dot{Q}_{rad}}{\dot{Q}_{rad}}\right)^2 &= \left(\frac{\Delta\dot{m}}{\dot{m}}\right)^2 + \left(\frac{\Delta\left(h_{T_{pL,out}} - h_{T_{pL,in}} - h_{T_{pH,in}} + h_{T_{pH,out}}\right)}{h_{T_{pL,out}} - h_{T_{pL,in}} - h_{T_{pH,in}} + h_{T_{pH,out}}}\right)^2 \\
\left(\frac{\Delta\dot{Q}_{rad}}{\dot{Q}_{rad}}\right)^2 &= \left(\frac{\Delta\dot{m}}{\dot{m}}\right)^2 + \left(\frac{\sqrt{\Delta h_{T_{pL,out}}{}^2 + \Delta h_{T_{pL,in}}{}^2 + \Delta h_{T_{pH,in}}{}^2 + \Delta h_{T_{pH,out}}{}^2}}{\Delta h_{pL} - \Delta h_{pH}}\right)^2 \\
\left(\frac{\Delta\dot{Q}_{rad}}{\dot{Q}_{rad}}\right)^2 &= \left(\frac{\Delta\dot{m}}{\dot{m}}\right)^2 + \left(\frac{\sqrt{\left[c_{p(pL,T_{out})}\Delta T\right]^2 + \left[c_{p(pL,T_{in})}\Delta T\right]^2 + \left[c_{p(pH,T_{in})}\Delta T\right]^2 + \left[c_{p(pH,T_{out})}\Delta T\right]^2}}{\Delta h_{pL} - \Delta h_{pH}}\right)^2 \\
\Delta\dot{Q}_{rad} &= \dot{Q}_{rad}\sqrt{\left(\frac{\Delta\dot{m}}{\dot{m}}\right)^2 + \left(\frac{\sqrt{\left[c_{p(pL,T_{out})}\Delta T\right]^2 + \left[c_{p(pL,T_{in})}\Delta T\right]^2 + \left[c_{p(pH,T_{in})}\Delta T\right]^2 + \left[c_{p(pH,T_{out})}\Delta T\right]^2}}{\Delta h_{pL} - \Delta h_{pH}}\right)^2}
\end{aligned} \tag{10.2}
$$